

Bursting and reformation cycle of the laminar separation bubble over a NACA-0012 aerofoil: Characterisation of the flow-field

Eltayeb M. ElJack^{1,*}, Ibraheem M. AlQadi², and Julio Soria^{2,3}

1 Mechanical Engineering Department, University of Khartoum, Khartoum, Sudan

2 Aeronautical Engineering Department, King Abdulaziz University, Jeddah, Saudi Arabia

3 Laboratory for Turbulence Research in Aerospace and Combustion, Department of Mechanical and Aerospace Engineering, Monash University, Melbourne, Australia

* emeljack@uofk.edu

Abstract

This study examines the effects of angle of attack on the characteristics of the laminar separation bubble (LSB), its associated low-frequency flow oscillation (LFO), and the flow-field around a NACA-0012 aerofoil at $Re_c = 5 \times 10^4$ and $M_\infty = 0.4$. In the range of the investigated angles of attack, statistics of the flow-field suggest the existence of three distinct angle-of-attack regimes: 1) the flow and aerodynamic characteristics are not much affected by the LFO for angles of attack $\alpha < 9.25^\circ$; 2) the flow-field undergoes a transition regime in which the bubble bursting and reformation cycle, LFO, develops until it reaches a quasi-periodic switching between separated and attached flow in the range of angles of attack $9.25^\circ \leq \alpha \leq 9.6^\circ$; and 3) for the angles of attack $\alpha > 9.6^\circ$, the flow-field and the aerodynamic characteristics are overwhelmed by a quasi-periodic and self-sustained LFO until the aerofoil approaches the angle of full stall. The length of the bubble, in the mean sense, decreases to a minimum size of 33.5% of the aerofoil chord at $\alpha = 9.0^\circ$ then it grows in size when the angle of attack is further increased. A trailing-edge bubble (TEB) forms at $\alpha > 9.25^\circ$ and grows with the angle of attack. The LSB and TEB merge and continue to deform until they form an open bubble at $\alpha = 10.5^\circ$. On the suction surface of the aerofoil, the pressure distribution shows that the presence of the LSB induces a gradual and continues adverse pressure gradient (APG) when the flow is attached. The bursting of the bubble causes a gradual and continues favourable pressure gradient (FPG) when the flow is separated. This is indicative that a natural forcing mechanism keeps the flow attached against the APG and separated despite the FPG. It is shown that perturbations of the wall-normal and the spanwise velocity components are extracted exclusively by the local velocity gradient inside the shear layer via the Kelvin–Helmholtz instability. Whereas, the fluctuations in the streamwise velocity component and the pressure are due to a global oscillation in the flow-field in addition to the velocity gradient across the shear layer. The variance of the pressure fluctuations has a significant magnitude in the laminar portion of the separated shear layer. This is indicative that the instability that generates and sustains the LFO originates at this location. The present investigation suggests that most of the observations reported in the literature about the LSB and its associated LFO are neither thresholds nor indicators for the inception of the instability, but rather are consequences of it.

1 Introduction

Interest in low Reynolds number aerodynamics, $Re_c = 10^4$ to 10^6 based on the free-stream velocity and aerofoil chord, has significantly increased over the past three decades. This is because of the steady increase in applications that operate at low Reynolds numbers due to high altitude flight, where the kinematic viscosity is relatively higher, and/or having small geometrical dimensions. The low Reynolds number aerodynamics of an aerofoil at incidence is characterised by its proclivity to induce a laminar separation bubble (LSB) on the upper surface of the aerofoil. Some of the known conditions for the formation of an LSB are functions of the Reynolds number of the flow, pressure distribution, aerofoil geometry, surface roughness, and turbulence intensity of the free-stream. Figure 1 shows an LSB over a NACA-0012 aerofoil at Reynolds number of 5×10^4

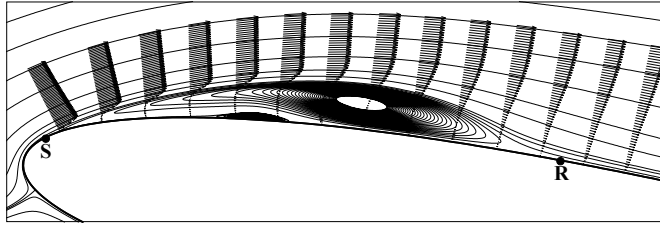


Figure 1. A laminar separation bubble over a NACA-0012 aerofoil at the angle of attack of 9.25° .

and the angle of attack of 9.25° .

At the leading-edge of the aerofoil, a laminar boundary layer is established by the incoming flow. The boundary layer remains laminar, if not forced into early transition, until the pressure gradient changes from negative to positive. If the adverse pressure gradient is strong, the laminar boundary layer detaches and travels away from the aerofoil surface to create a region of separated flow near the surface (point **S** in figure 1). Along the separated shear layer, kinetic energy is extracted from the mean flow and fed to the perturbations. The process of feeding energy into the 2D-rolls continue until they break down into three-dimensional structures and transition to turbulence initiates. Consequently, the flow reattaches because the boundary layer becomes more energetic (point **R** in figure 1). The flow is reversed in the region between points **S** and **R** in figure 1 which constitutes an LSB. Beneath the LSB lies a small counter-rotating bubble, which is called a *secondary bubble*. The turbulent boundary layer downstream of the bubble has more momentum near the surface to resist the adverse pressure gradient and avoid a new separation.

Owen & Klanfer (1953) classified the LSB into two distinct formats of short and long bubble. The bubble is short if the ratio of the bubble length to the displacement thickness at the point of separation is in the order of 100. Whereas, the bubble is termed long if the ratio is in the order of 400. A short bubble has little effect on the external potential flow, while the long bubble has a more notable influence. At certain conditions, short bubble suddenly alters to a long bubble or a fully separated flow without any subsequent reattachment which is termed as bubble bursting. Recent experimental and numerical observations have shown an unusual switching between bubble bursting and reattachment at a low frequency on the inception of stall (Rinoie & Takemura, 2004; Tanaka, 2004; Almutairi & Alqadi, 2013; Almutairi *et al.*, 2015; Eljack *et al.*, 2016; Almutairi *et al.*, 2017; Eljack, 2017).

Mccullough & Gault (1951) classified the aerofoil stall into three main categories: 1) leading-edge, 2) thin-aerofoil, and 3) trailing-edge stall. The leading-edge stall results from the flow separation near the leading-edge without any subsequent reattachment downstream of the separation. In the thin-aerofoil stall, the flow reattaches downstream the separation, and then the reattachment point moves toward the trailing-edge as the angle of attack increases. The trailing-edge stall initiates at the trailing-edge where the flow separates, and the separation point moves toward the leading-edge as the angle of attack increases. Gaster (1967) who was the first to systematically investigate the stability of the LSB, found that bubble bursting occurs either by a gradual increment in the bubble length or by a suddenly discontinuous event. The former applies in the present work as will be seen in § 3.

The instantaneous shape of the LSB is random, and an instantaneous continuous separation or reattachment line in the spanwise direction is not defined. A question was raised as to whether spanwise averaging of the data is justified, and before that, if the assumption of periodic flow in this direction is valid. The most important to us is the shape of the large-scale bubbles; are they two-dimensional? Previous works on two-dimensional aerofoil stalling characteristics have shown a low-frequency and highly unsteady flow or a steady large-scale three-dimensional structure. The latter is termed stall cells, and there was considerable amount of research focused on their structure. Winkelman & Barlow (1980) carried out an oil-flow visualisations of the flow-field on the suction surface of stalled wings of Clark Y aerofoil section at chord Reynolds numbers of 24.5×10^4 , 26×10^4 , and 38.5×10^4 . The ends of the wing are flush with the tunnel side walls or splitter plates and on plane rectangular wings of infinite aspect ratio. They observed that the mushroom-shaped cells started to form at the onset of stall on the two-dimensional model. The three-dimensional cells coexisted with trailing-edge stall cell on the surface of the wing several degrees above the stalling angle of attack. They tentatively sketched a flow-field model showing the general features of a leading-edge separation bubble and trailing-edge separation. Winkelman (1990) took up Winkelman & Barlow (1980) work and measured the spectra of the velocity in the wake of a rectangular wing having the same aerofoil section. The spectra of the

wake measurements did not show any indications of a dominant low-frequency mode. Yon & Katz (1998) used fine-thread tuft-flow visualisation and high-frequency response pressure transducers measurements to investigate the unsteady features of the stall cells. They studied the flow-field around a wing of aspect ratio ranging from 2 to 6 with the NACA-0015 aerofoil section. They imposed the two-dimensionality by using end plates that effectively eliminated the tip flow. The authors reported the existence of a low-frequency mode in their pressure spectra, but with considerably smaller amplitudes of oscillations. Broeren & Bragg (2001) studied five different aerofoil configurations (NACA-2414, NACA-64A010, LRN-1007, E374 and Ultra-Sport) by measuring the wake velocity across the spanwise direction, and using mini-tufts for flow visualisation. They found that all the stall types were dependent on the type of the aerofoil. They concluded that the low-frequency flow oscillation (LFO) phenomenon always occurs in the aerofoils that exhibits a thin-aerofoil stall or the combination of both thin-aerofoil and trailing-edge stall. Most importantly to us, they found that the low-frequency unsteadiness is essentially two dimensional. Their conclusions were in good agreement with that of Zaman *et al.* (1989) who observed that the LFO takes place with aerofoils exhibiting either the trailing-edge or thin-aerofoil type stalls but does not take place with the leading-edge type stall. To this end, it is evident that the LFO phenomenon is inherently two-dimensional by its nature and neither the imposed boundary condition nor the spanwise averaging affected the results presented in § 3.

Eljack (2017) showed that at relatively low angles of attack, the LSB is present on the upper surface of an aerofoil and remains intact. As the angle of attack of the aerofoil is increased to a critical value, the LSB abruptly and intermittently bursts, which causes an oscillation in the flow-field and consequently the aerodynamic forces. As the angle of attack is increased above the critical angle, the bursting becomes more frequent, and the LSB exhibits a quasi-periodic switching between long and short bubbles, which results in a global LFO. As the aerofoil approaches the full stall angle, the flow remains separated with intermittent and abrupt random reattachments. The aerofoil eventually undergoes a full stall as the angle of attack is further increased.

The presence of the bubble significantly deteriorates the aerodynamic performance, such as loss of lift, undesirable change in the moment, and increase in the drag. Flow oscillations due to bubble shedding and sudden aerofoil stalling due to bubble bursting are direct consequences of the complex and random behaviour of the LSB. The ultimate goal is to control the flow-field around an aerofoil at low Reynolds numbers in the presence of an LSB to improve its performance. However, very little of the general character of the LSB is understood. Revealing the underlying mechanism behind the self-sustained periodic bursting and reformation of the bubble is an essential step towards control of its undesirable effects.

The objective of the present study is to examine the effects of the angle of attack on the characteristics of the LSB, its associated LFO, and the flow-field around a NACA-0012 aerofoil at $Re_c = 5 \times 10^4$ and $M_\infty = 0.4$. A conditional time-averaging is used to characterise the flow-field. The characteristics of the flow-field, the LSB, and the LFO are provided along with careful comparisons with existing experimental and numerical work. Similarities are discussed in detail and discrepancies are justified wherever necessary.

2 Mathematical modelling and computational setup

The non-dimensional Favre-filtered compressible Navier–Stokes equations in curvilinear coordinates are given by:

$$\frac{\partial \bar{\rho}}{\partial t} + \frac{\partial}{\partial \xi_j} \left[\dot{\xi}_{ij} (\bar{\rho} \tilde{u}_j) \right] = 0 \quad (1)$$

$$\frac{\partial}{\partial t} (\bar{\rho} \tilde{u}_i) + \frac{\partial}{\partial \xi_j} \left[\dot{\xi}_{ij} (\bar{\rho} \tilde{u}_i \tilde{u}_j + \bar{p} \delta_{ij} - \tilde{\sigma}_{ij}) \right] = - \underbrace{\frac{\partial}{\partial \xi_j} (\dot{\xi}_{ij} \tau_{ij})}_{(1)} + \underbrace{\frac{\partial}{\partial \xi_j} [\dot{\xi}_{ij} (\bar{\sigma}_{ij} - \tilde{\sigma}_{ij})]}_{(2)} \quad (2)$$

$$\frac{\partial}{\partial t} (\bar{\rho} \tilde{E}) + \frac{\partial}{\partial \xi_j} \left[\dot{\xi}_{ij} \left((\bar{\rho} \tilde{E} + \bar{p}) \tilde{u}_j + \tilde{q}_j - \tilde{\sigma}_{ij} \tilde{u}_i \right) \right] = - \underbrace{\frac{\partial}{\partial \xi_j} [\dot{\xi}_{ij} (Q_j + \frac{1}{2} \mathcal{G}_j - \mathcal{D}_j)]}_{(3)} \quad (3)$$

Where, \tilde{u}_i is the velocity component in the x_i direction, \tilde{p} is the pressure, $\tilde{\rho}$ is the density, \tilde{T} is the temperature, and \tilde{E} is the total energy per unit mass. The stress tensor is given by:

$$\sigma_{ij} = \frac{2\tilde{\mu}}{Re} S_{ij} - \frac{2\tilde{\mu}}{3Re} \delta_{ij} S_{kk}, \quad S_{ij} = \frac{1}{2} \left(\frac{\partial u_i}{\partial \xi_j} \frac{\partial \xi_j}{\partial x_i} + \frac{\partial u_j}{\partial \xi_i} \frac{\partial \xi_i}{\partial x_j} \right) \quad (4)$$

The heat flux vector is given by:

$$\tilde{q}_j = \frac{\tilde{\mu}}{(\gamma - 1)\text{Re Pr } M_\infty^2} \frac{\partial \tilde{T}}{\partial \xi_j} \frac{\partial \xi_j}{\partial x_i} \quad (5)$$

where

$$\tilde{\mu} = \tilde{T}^{\frac{3}{2}} \frac{1 + C}{\tilde{T} + C}, \quad (C = 0.3686), \quad \tilde{T} = \gamma M_\infty^2 \frac{\bar{p}}{\bar{\rho}} \quad (6)$$

ξ_{ij} is the transformation metrics tensor given by:

$$\xi_{ij} = \frac{1}{J} \frac{\partial \xi_j}{\partial x_i}, \quad J = \left| \frac{\partial x_i}{\partial \xi_j} \right| \quad (7)$$

The Favre-filtered equations consist of the terms from the Navier–Stokes equations on the left hand side, in addition to the terms on the right hand side resulting from the filtering operation. The under-bracketed terms represent the effects of the unresolved subgrid-scale (sgs) turbulent structures. τ_{ij} is the sgs stress tensor ($\tau_{ij} = \bar{\rho}(\overline{u_i u_j} - \tilde{u}_i \tilde{u}_j)$), Q_j is the sgs heat flux vector ($Q_j = \bar{\rho}(\overline{u_j T} - \tilde{u}_j \tilde{T})$), and $\partial \mathcal{G}_j / \partial x_j$ is the sgs turbulent diffusion term, where $\mathcal{G}_j = \bar{\rho}(\overline{u_j u_k u_k} - \tilde{u}_j \overline{u_k u_k})$ is the sgs viscous diffusion term and $\mathcal{D}_j = \overline{\sigma_{ij} u_i} - \tilde{\sigma}_{ij} \tilde{u}_i$. The nonlinear sub-filter viscous contribution, term (2) in equation 2, is from the use of \tilde{T} to evaluate $\mu(\tilde{T})$. This term is very small and negligible compared to (1) in the same equation. Similarly, the sgs viscous diffusion term $\partial \mathcal{D}_j / \partial x_j$ is also neglected. The sgs heat flux vector Q_j and sgs turbulent diffusion term $\partial \mathcal{G}_j / \partial x_j$ are negligible for low Mach number flows Vreman (1995).

The sgs stress tensor τ_{ij} represents the effect of the small-scale turbulent structures and is defined as:

$$\tau_{ij} = \bar{\rho}(\overline{u_i u_j} - \tilde{u}_i \tilde{u}_j) \quad (8)$$

The sgs stress tensor τ_{ij} is modelled by using the eddy viscosity concept under the low compressibility:

$$\tau_{ij} - \frac{1}{3} \delta_{ij} \tau_{kk} = 2\nu_t \tilde{S}_{ij} \quad (9)$$

where τ_{kk} refers to the trace of the sgs Reynolds stress tensor and ν_t refers to the turbulent eddy viscosity obtained by the mixed-time-scale (mts) model developed by Inagaki *et al.* (2005). The model is turned off automatically in the laminar flow region. Thus, it overcomes the drawbacks of using a wall-damping function. In this model, the eddy viscosity is calculated by using the following definition:

$$\nu_t = C_{\text{mts}} \tau_s k_{\text{sgs}} \quad (10)$$

where C_{mts} refers to the model fixed parameter. τ_s refers to the time scale given by:

$$\tau_s^{-1} = \left(\frac{\bar{\Delta}}{\sqrt{k_{\text{sgs}}}} \right)^{-1} + \left(\frac{C_\tau}{|\bar{S}|} \right)^{-1} \quad (11)$$

where

$$|\bar{S}| = \sqrt{2\bar{S}_{ij}\bar{S}_{ij}}, \quad \bar{\Delta} = (\Delta x_1 \Delta x_2 \Delta x_3)^{\frac{1}{3}} \quad (12)$$

$\bar{\Delta}$ refers to the filter size, and C_τ is the time-scale parameter. The velocity scale k_{sgs} is defined by:

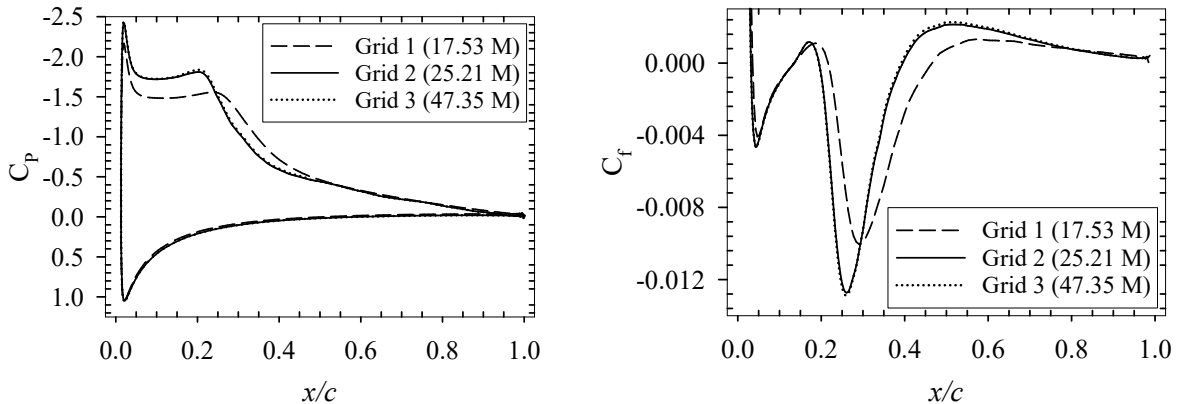
$$k_{\text{sgs}} = (\bar{u} - \hat{u})^2 \quad (13)$$

As long as the flow is fully resolved, the above definition gives a zero velocity scale in the laminar flow region. Consequently, the eddy viscosity (ν_t) also approaches zero in this region.

The LES code utilised in the present simulations is an LES version of the direct numerical simulation (DNS) code written and validated by Jones *et al.* (2010). The Navier–Stokes equations were discretised using a fourth-order explicit central difference scheme for spatial discretisation in the interior points. The fourth-order boundary scheme of Carpenter *et al.* (1999) was used to treat points near and at the boundary. To preserve the spatial characteristics, the transformation metrics tensor ξ_{ij} was evaluated by using the same fourth-order scheme. Temporal discretisation is performed using a low-storage fourth-order Runge–Kutta scheme. The solution stability was improved by implementing an entropy splitting scheme Sandham & Yee (2001). The

Table 1. Computational grid parameters

Grid	y^+	Δx^+	Δz^+	N_ξ	N_η	N_ζ	Total points
Grid-1	> 1	< 50	< 50	637	320	86	17, 530, 240
Grid-2	< 1	< 15	< 15	780	320	101	25, 209, 600
Grid-3	< 1	< 10	< 10	980	320	151	47, 353, 600

**Figure 2.** Sensitivity of the mean pressure coefficient and the mean skin-friction coefficient to grid refinement at the angle of attack $\alpha = 9.25^\circ$.

entropy splitting constant β was set equal to 2.0 Jones (2008). The combination of a relatively coarse grid and high-order scheme results in the generation of spurious high-frequency waves. The non-physical waves will contaminate the solution if they are not eliminated at each time step. Thus, the solution must be filtered to eliminate spurious waves at the high unresolved wavenumber range by damping their amplitude with minimal effect on the resolved waves at lower wavenumbers. The filtering scheme used here is a fourth-order compact scheme developed by Gaitonde & Visbal (1998). The integral characteristic boundary condition is applied at the free-stream and the far-field boundaries Sandhu & Sandham (1994). The zonal characteristic boundary condition is applied at the downstream exit boundary Sandberg & Sandham (2006) which are considered as non-reflected boundary conditions to overcome the circulation effects at the boundaries. The adiabatic and no-slip conditions are applied at the aerofoil surface. The LSB, its associated LFO, and the flow-field are inherently two dimensional. Therefore, a periodic boundary condition is applied in the spanwise direction for each step of the Runge-Kutta time steps. The internal branch-cut boundary was updated at each step of the Runge-Kutta scheme.

In terms of the aerofoil chord (c), the dimensions of the computational domain were set as follows: $W = 5.0c$ in the wake region, from the aerofoil trailing-edge to the outflow boundary in the streamwise direction; $L_\eta = 7.3c$ in the wall-normal direction (the C-grid radius); and $L_\zeta = 0.5c$ in the spanwise direction. Where ξ, η and ζ are the curvilinear coordinates along the aerofoil surface, in the wall-normal direction, and the spanwise direction, respectively.

A grid sensitivity study was performed to assess the effect of the grid distribution on the characteristics of the LSB and its associated LFO. Three different grid distributions were used; a coarse grid (Grid-1) with the dimensions of $N_\xi \times N_\eta \times N_\zeta = 637 \times 320 \times 86$, a fine grid with the dimensions of $780 \times 320 \times 101$ (Grid-2), and a finer grid with the dimensions of $980 \times 320 \times 151$ (Grid-3). Table 1 shows summary of the three different grids. Grid-2 is a refined and optimised version of Grid-1 by redistributing grid points in the η direction such that around 60% of the total grid points were within one chord from the aerofoil surface. Grid-2 and Grid-3 were generated using a hyperbolic grid generator to improve the grid orthogonality and minimise the grid skewness. The wall-normal grid spacing was reduced to ensure a wall-normal spacing of $y^+ \leq 1$. Having inadequate spacing in the ξ direction could affect the development of the evolving Kelvin-Helmholtz instability and consequently the transition process. Equidistant grid spacing with a relatively small Δx was adopted in the range $0 \leq x/c \leq 0.5$ for Grid-2 and Grid-3. The number of grid points in the spanwise direction was increased from 86 grid points in Grid-1 to 101 grid points in Grid-2, and 151 grid points in

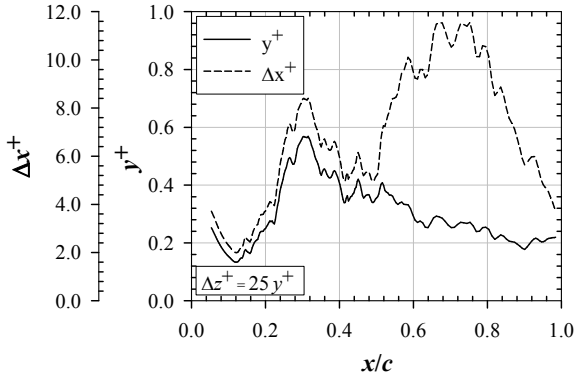


Figure 3. Grid resolution, attached-phase.

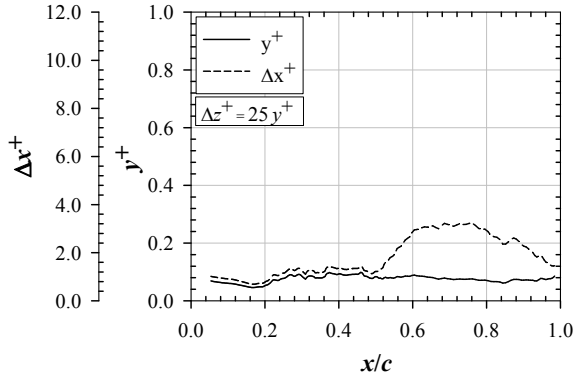


Figure 4. Grid resolution, separated-phase.

Grid-3. This has reduced the grid spacing in viscous wall units to less than 15 and significantly improved the solution. An adequate grid distribution in the spanwise direction is crucial for the break-down of the evolving Kelvin–Helmholtz instability. Thus, predicting the correct location of transition depends on the grid distribution.

Figure 2 shows the mean pressure and mean skin-friction coefficients for Grid-1, Grid-2, and Grid-3. The averaged pressure coefficient distribution on the aerofoil suction side for Grid-2 has a much stronger adverse pressure near the leading edge. For the mean skin-friction coefficient, the bubble size was smaller in Grid-2 case. In contrast, it was a bit longer in the coarse grid case (Grid-1). The bubble characteristics are independent of the grid at a grid resolution higher than that of Grid-2 as seen in the figure. As seen in the figure, the differences in the mean pressure and mean skin-friction distributions for Grid-1 and Grid-2 are huge compared to the small change in the overall grid points. However, the difference in Grid-1 and Grid-2 is not only in the number of grid points, but also in the quality of the grid. Grid-1 contains high skewed cells, the grid points are not adequately distributed in the wall-normal direction, and the grid is stretched in the streamwise direction. On the contrary, Grid-2 is optimized to have orthogonal cells and minimum skewness. Moreover, the grid points are optimally distributed in the wall-normal direction such that the grid points are intensified near the wall and along the shear layer. Also, an equidistance grid distribution is employed in the transition region. Finally, the number of grid points is significantly increased in the spanwise direction which enhanced the prediction of the break-down of the evolving Kelvin–Helmholtz instability and the transition location. Thus, the mean pressure coefficient and mean skin-friction coefficient have huge difference despite the relatively small change in the number of grid points.

For the aerodynamic forces, the grid sensitivity study showed that the LFO was always captured whether the coarse or fine grid is used. However, when coarse grids is used, the LFO is captured at lower angles of attack. As the grid is refined, the LFO is captured at slightly higher angles of attack. When an adequate grid distribution is used, the angle of attack at which the LFO takes place becomes independent of the grid resolution. This explains why Mukai *et al.* (2006) observed several aspects of the LFO phenomenon despite using a much coarser grid.

An investigation was performed to assess the effect of the domain spanwise width on the characteristics of the LSB and its associated LFO phenomena. Five spanwise widths of $L_\zeta = 0.2c, 0.25c, 0.5c, 0.75c,$ and $1.0c$ were considered. The mean skin-friction coefficient and the mean pressure coefficient showed that the shape and length of the LSB are independent of the computational domain width for $L_\zeta \geq 0.25c$. Therefore, a domain width of $L_\zeta = 0.5c$ was considered sufficient for the current Reynolds number. A computational grid with the dimensions $N_\xi \times N_\eta \times N_\zeta = 780 \times 320 \times 101$ was generated around a NACA-0012 aerofoil for each of the sixteen angles of attack. The aerofoil was oriented such that the incoming free-stream was always at a zero angle. Figures 3 and 4 show the grid resolution at the aerofoil surface for the attached and separated phases of the LFO cycle at $\alpha = 9.8^\circ$. The figures illustrate the variation of y^+ in the η direction, Δx^+ in the ξ direction, and Δz^+ in the ζ direction on the aerofoil suction side. The maximum grid spacing values for the wall-normal units during the attached phase were $y^+ = 0.55$, $\Delta x^+ = 12$, and $\Delta z^+ = 14$ with 20 grid points within $y^+ \leq 10$. y^+ had relatively high values in the range $0.2 \leq x/c \leq 0.4$; this is the region where the transition to turbulence takes place. The maximum grid spacing is smaller for the separated phase because the velocity gradient is much smaller in this case.

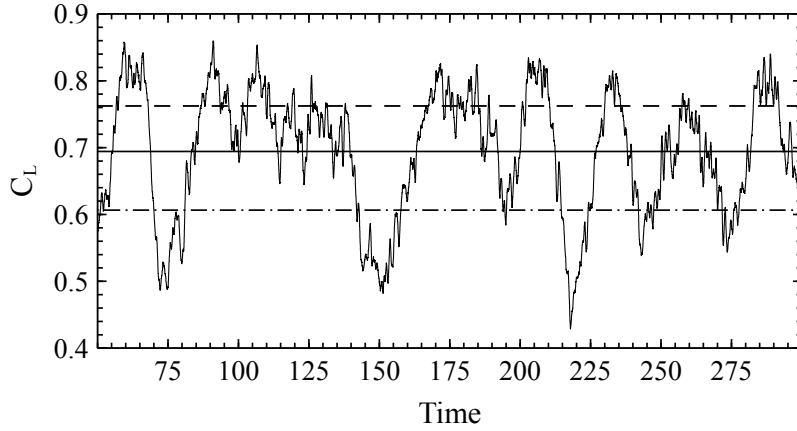


Figure 5. Time history of the lift coefficient at the angle of attack 9.80° plotted versus non-dimensional time. Solid line: mean ($\overline{C_L}$), dashed line: high-lift mean ($\widehat{C_L}$), and dash-dot line: low-lift mean ($\widetilde{C_L}$).

3 Results and discussion

LESs were carried out for the flow around the NACA-0012 aerofoil at sixteen angles of attack ($\alpha = 9.0^\circ$ – 10.1° at increments of 0.1° as well as $\alpha = 8.5^\circ$, 8.8° , 9.25° , and 10.5°). The simulation Reynolds number and Mach number were $Re_c = 5 \times 10^4$ and $M_\infty = 0.4$, respectively. The free-stream flow direction was set parallel to the horizontal axis for all simulations ($u = 1$, $v = 0$, and $w = 0$). The entire domain was initialised using the free-stream conditions. The simulations were performed with a time step of 10^{-4} non-dimensional time units. The samples for statistics are collected once transition of the simulations has decayed and the flow became stationary in time after 50 flow-through times which is equivalent to 50 non-dimensional time units. Aerodynamic coefficients (lift coefficient (C_L), drag coefficient (C_D), skin-friction coefficient (C_f), and moment coefficient (C_m)) were sampled for each angle of attack at a frequency of 10,000 to generate two and a half million samples over a time period of 250 non-dimensional time units. The locally-time-averaged and spanwise ensemble-averaged pressure, velocity components, and Reynolds stresses were sampled every 50 time steps on the x - y plane. A dataset of 20,000 x - y planes was recorded at a frequency of 204 at each angle of attack.

3.1 Conditional time-averaging

The signal of the lift coefficient at each angle of attack was used as a reference for conditionally time-averaging the flow-field. The time-average of an instantaneous variable of the flow-field, ψ , was defined on three different levels: 1) a mean-lift average; 2) a high-lift average in which the flow-field is attached in the statistical sense; and 3) a low-lift average in which the flow is statistically separated. The mean-lift average of the variable, $\overline{\psi}$, is simply the time-average of all data samples of the variable. The high-lift average of the variable, $\widehat{\psi}$, is the time-average of all data samples that have values higher than the mean values. The low-lift average of the variable, $\widetilde{\psi}$, is the average of all data samples that have values less than the mean values. The lift coefficient signal is used to identify the data samples that are above or below the mean. It is implemented by taking the mean of the lift coefficient at each angle of attack. The indices of data points of the time-history of the lift coefficient that are above/below the mean of the lift coefficient are then stored in a high-lift/low-lift data files, respectively. The indices are then used to locate the data of other flow variables that are above/below their corresponding mean and consequently used to estimate the low-lift and high-lift time-average for all of the flow variables. Figure 5 illustrates the concept of the conditional time-averaging that is based on the lift coefficient.

3.2 Mean flow

The first observations and descriptions of the LSB were reported by Melvill Jones (1934a) and Melvill Jones (1934b). After that, the structure of the LSB was investigated in the work of Young & Horton (1966) and its averaged shape was described by Horton (1968). Since then, many experimental measurements were

conducted on the suction surface of different aerofoils. In most of the previous works, it was observed that the length of the LSB decreases as the angle of attack is increased. At a critical angle of attack, the shortest bubble is achieved, and the LSB length increases when the angle of attack is increased above the critical angle.

Figures 6, 7, and 9 show streamlines patterns superimposed on colour maps of the streamwise velocity component of the mean, high-lift, and low-lift flow-fields, respectively, at the angles of attack $\alpha = 9.25^\circ$ – 10.5° . As seen in the figures, the LSB is formed on the upper surface of the aerofoil. The bubble length, height, and shape varies as the angle of attack is increased. It is noted that the flow is fully attached, in the mean sense, in the three figures at the angle of attack of 9.25° . The flow is massively separated, open bubble, in the three figures at the angle of attack of 10.5° . This is indicative that these two angles set the limits of the angles of attack of interest.

Figure 9 shows that a trailing-edge separation region that constitutes a trailing-edge bubble (TEB) is formed at angles of attack $\alpha > 9.25^\circ$ and continues to grow as the angle of attack is increased. At the angle of attack of 9.7° the leading-edge and the trailing-edge bubbles merge. The merged bubbles continue to deform until an open bubble is formed at the angle of attack of 10.5° . This type of stall is a combination of thin-aerofoil and trailing-edge stall as classified by McCullough & Gault (1951). This process occurs at the same sequence of events but at higher angles of attack for the high-lift mean, figure 7, and at lower angles of attack for the mean, figure 6.

Broeren & Bragg (1999) studied the flow-field around an LRN(1)–1007 aerofoil at $Re_c = 3 \times 10^5$ and an angle of attack $\alpha = 15^\circ$. Two velocity components were measured at 687 locations in the x – y plane at the aerofoil mid-span using laser Doppler velocimeter (LDV). A Conditional-averaging method was used and 24 time slots within one cycle resolved the oscillation in 15° intervals. They showed four snapshots of contours of the streamwise velocity at four different phases. The snapshots show small leading-edge and trailing-edge separated zones, they grow in the second snapshot, merge in the third one, and become an open bubble in the fourth snapshot. Their experimental observations are in good agreement with the present discussion inequities of how limited and coarse their data is.

It is interesting to note that the secondary bubble exists at the same location when the flow is attached and when it is massively separated. This is indicative that the secondary bubble plays a profound role in the underlying mechanism behind the self-sustained quasi-periodic low-frequency switching between attached and separated flow. Furthermore, the current observation being statistical implies that the secondary bubble and the conditions for its formation are permanent in space and stationary in time. To the best of the authors' knowledge, this has never been observed in any of the previous work.

Figure 8 illustrates the mean length and the mean height of the LSB and the TEB plotted versus the angle of attack. The mean length and height of the bubbles were obtained by approximating the locations of separation and reattachment for each bubble from the streamlines patterns. At relatively low angles of attack, before the merging of the two bubbles, the LSB and TEB are bounded by four half-saddle points. The first half-saddle point is the separation point at the vicinity of the leading-edge (**SP1**). The second half-saddle point is the reattachment point located just downstream the LSB (**SP2**). The third half-saddle is the separation point near the trailing-edge (**SP3**). The fourth half-saddle point is the reattachment point located at the trailing-edge (**SP4**). The first two half-saddle points constitute the LSB, and the latter two half-saddle points constitute the TEB. At relatively high angles of attack, when the two bubbles start to merge, the two half-saddle points **SP2** and **SP3** move away from the wall and form a full-saddle point (**SP**). The LSB and TEB are bounded by two half-saddle points and the newly formed full-saddle point: **SP1**, **SP**, and **SP4**. The length of the LSB is measured from **SP1** to **SP** and the length of the TEB is measured from **SP** to **SP4**. The size of the mean bubbles grows with the angle of attack. When the LFO become fully developed, the length of the LSB starts to decrease as the angle of attack is increased and the summation of the LSB and TEB length spans the whole aerofoil chord. The height of the bubbles is measured across each bubble from the aerofoil surface, passing through the bubble focus, and to the edge of the bubble. As shown in figure 8 (right), the height of the bubbles increases with the angle of attack.

The separated shear layer is highly unstable, but a distinction needs to be drawn between convective instability, where disturbances grow in space, and absolute instability where disturbances grow in time. Most of the work pegs the stability of the bubble to changes in the separated shear layer and its associated Kelvin–Helmholtz instability. Analysis performed by Nieu (1993) for backward facing step flows suggests absolute instability for flow with more than 20% reverse flow. Whereas, Hammond & Redekopp (1998) predicted 30% for the start of absolute instability in LSBs. Figure 10 shows the variation of the maximum reverse velocity (MRV) inside the bubble as a percentage of the free-stream velocity, denoted by circles, and as a percentage of the maximum

external velocity outside the bubble, denoted by \times 's. The MRV reach a maximum of 22% of the maximum external velocity outside the bubble and a maximum of 35.6% of the free-stream velocity at the angle of attack of 9.0° . The location of the MRV is shown on the right-hand side of figure 10. The circles denote the location of MRV in x direction measured from the aerofoil leading-edge and the \times 's denote the location of the MRV in the y direction measured from the aerofoil surface. At the angles of attack of $9.0^\circ \leq \alpha \leq 9.25^\circ$ the location of the MRV was about 0.236 chords downstream the leading-edge. At higher angles of attack, the location of the MRV moved downstream. The location of the MRV in y direction moves away from the aerofoil surface when the angle of attack is increased. The study by Alam & Sandham (2000) showed that the separation bubble is considered absolutely unstable if the separation bubble sustains a maximum reverse velocity percentage in the range $MRV = 15\%$ to 20% . The MRV for the current simulation, 22%, is larger than the range pointed out by Alam & Sandham (2000) and can be considered as an indication of the presence of an absolute instability in the bubble. However, it is not clear yet whether the threshold of the MRV is an indication of the inception of the absolute instability or it is a consequence of the absolute instability for the current configuration. That is, is this threshold a necessary or a sufficient condition for the absolute instability. All previous observations, including the present study, reported the threshold as a necessary condition but it was never established if it is a sufficient condition. Therefore, it is concluded that the threshold of the MRV is an observation accompanying the LSB being absolutely unstable, but it is not the root cause that triggers the instability.

Contours plots of the mean pressure distributions around the aerofoil (\bar{p}) is illustrated in figure 11. The maximum contour level is set equal to the far-field pressure which is equal to 4.46 for the current configuration. It is noted that—on the suction surface of the aerofoil—the high-lift pressure in the vicinity of the LSB is lower than the mean pressure at the same location. Thus, the presence of the bubble induces an APG along the aerofoil chord when the flow is attached. It is also noted that, the low-lift pressure is higher than the mean pressure at the region of the LSB. Hence, the pressure gradient is favourable along the aerofoil chord when the flow is separated. This changes what is continuously reported in the literature that the bubble bursts because of the APG and the flow reattach because the early transition adds more energy to the boundary layer helping it overcome the APG and avoids new separation. In the light of the new observations, it seems that there is a natural forcing mechanism, instability, that forces the flow to remain attached against the APG and forces it to separate despite the FPG. Such a natural forcing mechanism seems to add momentum to the boundary layer during the attached flow phase and subtract momentum from the boundary layer during the separated flow phase.

At zero angle of attack, a reversed flow region exists on both sides of the aerofoil in the vicinity of the trailing-edge. These are consequences of the von Karman alternating vortices that shed at the wake of the aerofoil. For symmetric aerofoils at zero angle of attack, the von Karman vortices are mirror symmetric. However, as the angle of attack increases the upper vortex becomes larger and stronger than the lower one. At a critical angle of attack, the lower reversed flow region and the APG disappear and is replaced by an FPG. As seen in figure 11, at the angle of attack of 9.25° there is a small APG region on the pressure surface of the aerofoil. At higher angles of attack, this region is replaced by an FPG. The disappearance of the APG region on the pressure surface of the aerofoil might affects the dynamics of the flow and alters the oscillating flow mode at the trailing-edge. However, further investigation on the dynamics of the flow is required before such a conclusion can be drawn.

3.3 Turbulent kinetic energy

Most of the cited studies attribute the instability of the LSB to the process of transition to turbulence along the separated shear layer. These studies start by connecting the transition process to some type of linear instability via a Tollmien-Schlichting instability in the boundary layer or a Kelvin-Helmholtz instability in the separated shear layer above the LSB. Since velocity profiles in the separated region possess an inflection point, amplification of the two-dimensional disturbances is often attributed to the latter type of instability. The most widely accepted theory is that during the separated phase of the LFO cycle, acoustic waves due to the intense vortex shedding at the trailing-edge propagate upstream and generate hydrodynamic disturbances, several orders of magnitude larger than the acoustic disturbances Jones *et al.* (2010). Amplification of these disturbances within the laminar separated shear layer near the leading-edge forces earlier transition, and causing the flow to reattach. As the flow attaches, the strong vortex shedding at the trailing-edge dies down, and the acoustic feedback is cut-off. Hence, the transition is delayed, and the flow eventually separates. This self-sustained process repeats itself in a periodic manner.

Marxen *et al.* (2007) and Marxen & Henningson (2008) studied bubble bursting and how it is related to aerofoil stall. They hypothesised that changes in the transition process and the viscous-inviscid interaction both had a major role in bubble bursting. They performed a systematic study of bubble response to incoming disturbances, and they concluded that bubble bursting occurs when incoming disturbances are switched off. They hypothesised that bursting takes place when saturated disturbances cannot drive the flow to reattach. Recently, Alferez *et al.* (2013) studied the mechanism by which the LSB bursts and causes stall. They concluded that the bursting process is due to a change in the stability characteristics of the separated shear layer rather than a change of the instability mode from convective instability to absolute instability. Furthermore, Almutairi & Alqadi (2013) have shown that the location of transition moves downstream and away from the aerofoil surface during bubble bursting and upstream and close to the aerofoil surface during the reformation of the separation bubble. Almutairi *et al.* (2015) and Almutairi *et al.* (2017) applied Dynamic Mode Decomposition (DMD) to the pressure field of the flow around a NACA-0012 at $Re_c = 1.3 \times 10^5$, $M_\infty = 0.4$, and at the angle of attack of 11.5° . They concluded that the trailing-edge shedding generates acoustic waves that travel upstream and force early transition. The authors have suggested that the frequency of the trailing-edge shedding can be used to remove the LFO through periodic forcing. Eljack (2017) has shown, qualitatively, that the location of transition is connected to the trailing-edge shedding. However, in neither of these works it was established that the strong trailing-edge shedding is the necessary and sufficient condition for the early/late transition.

Before diving into the details of the changes inside the separated shear layer and how it affects the stability of the LSB, the authors would like to clarify the nature of the kinetic energy to be discussed. Amplification of small perturbations and extraction of energy from the mean flow and feeding it into the fluctuations does not mean that the flow undergoes transition to turbulence. In other words, three-dimensionality and several spectral tones of the fluctuations do not imply that the flow is turbulent. Therefore, the kinetic energy will be discussed in this context unless stated otherwise. The transition location as to early and late transition will be discussed in the context of the location of the maximum turbulent kinetic energy or the location of the maximum variance of a specific flow variable.

Figures 12, 13, and 14 illustrate the mean, high-lift, and low-lift variance of the streamwise velocity component, $\overline{u''^2}$, $\widehat{u''^2}$, and $\underline{u''^2}$, respectively. At the angle of attack of 9.25° , the distribution of $\overline{u''^2}$ coincides with the separated shear layer and the reattachment region. The bubble is intact, and the location of the maximum $\overline{u''^2}$ is just downstream the maximum bubble height. As the angle of attack is increased, the maximum magnitude of $\overline{u''^2}$ decreases, and its location moves downstream and away from the aerofoil surface. For the case of the attached flow, in the mean sense, $\widehat{u''^2}$ have higher values compared to its corresponding $\overline{u''^2}$. The locations of the maximum values of $\widehat{u''^2}$ are closer to the aerofoil surface and are located upstream their corresponding $\overline{u''^2}$ locations. As for the mean separated flow, the magnitudes of $\underline{u''^2}$ are lower than their $\overline{u''^2}$ counterparts. The maximum values of $\underline{u''^2}$ has less magnitude and locates further away from the aerofoil surface and downstream their corresponding $\overline{u''^2}$. It is noted that as the angle of attack is increased, the fluctuation level of the streamwise velocity component increases significantly in the vicinity of the trailing-edge as can be seen in figure 14. The oscillations are intensified during the separated phase (figure 14) and die down during the attached phase (figure 13). This is in total agreement with previous investigations Jones *et al.* (2010), Almutairi & Alqadi (2013), Almutairi *et al.* (2017), and Eljack (2017). However, does this implies that this is a sufficient condition for the instability of the LSB? This study found no proof that this condition being sufficient for the instability of the LSB. However, this is a strong indication that the instability behind the LFO is in action.

Figure 15 (left) shows the maximum values of $\overline{u''^2}$ plotted versus the angle of attack. As seen in the figure, $\overline{u''^2}$ increases linearly and sharply with the angle of attack and reaches a maximum at $\alpha = 9.4^\circ$. After that, $\overline{u''^2}$ decreases linearly as the angle of attack is further increased with systematic jumps at consistent intervals. The locations of the maximum $\overline{u''^2}$ are plotted versus the angle of attack as illustrated in the right-hand side of figure 15. $\Delta x/c$ is the distance measured from the aerofoil leading-edge in x direction, and $\Delta y/c$ is the distance measured from the aerofoil surface in y direction. It is noted that the location of the maximum $\overline{u''^2}$ moves away from the aerofoil surface as the angle of attack is increased. As for the distance in the x direction, it is found that the location of the maximum $\overline{u''^2}$ moves slowly towards the leading-edge and becomes closest to it at $\alpha = 9.25^\circ$. After that, the location of the maximum $\overline{u''^2}$ moves downstream. Again, this is in total agreement with previous studies. However, it is discussed here as a collateral outcome of the instability rather

than being the reason that triggers the instability.

The distributions of the variance of the wall-normal velocity component, $\overline{v''^2}$, are qualitatively and quantitatively different than their corresponding streamwise component, as seen in figures 16, 17, and 18. In the case of $\overline{u''^2}$, the variance has significant magnitude over all of the suction surface of the aerofoil including the boundary layer and the separated shear layer. At the trailing-edge, the streamwise velocity fluctuations have considerable amplitude. Whereas in the $\overline{v''^2}$ case, the fluctuations are significant away from the aerofoil surface and further downstream towards the trailing-edge. This is indicative that $\overline{u''^2}$ is the driving component in the separated flow in the chord-wise direction, whereas, $\overline{v''^2}$ act as a modulator of the reversed flow with no flapping in the wall-normal direction. It is also noted that the level of fluctuations of $\overline{v''^2}$ at the trailing-edge is comparable to that in the vicinity of the leading-edge. The oscillating mode is mostly attributed to the fluctuations in the wall-normal direction.

Figure 19 (left) shows that $\overline{v''^2}$ reaches a maximum value at the angle of attack of 9.25° . This is considerably lower than the angle of maximum $\overline{u''^2}$. The distances of the location of the maximum $\overline{v''^2}$ measured in x direction from the leading-edge and in y direction measured from the aerofoil surface are shown in the right-hand side of figure 19. These distances mimic those of $\overline{u''^2}$. The variance of the spanwise velocity component is similar to that of the wall-normal direction both quantitatively and qualitatively as seen in figure 20. The flow in this direction is periodic. Hence, the mean velocity component in this direction is zero. The only acting velocity in this direction is the spanwise perturbations. These are responsible for the break-down of the two-dimensional rolls into three-dimensional structures.

The conditional time-averaging employed in the present study does not distinguish the small-scale perturbations, “turbulence”, from oscillations induced by large-scale vortices. However, the behaviour of both $\overline{v''^2}$ and $\overline{w''^2}$ coincides with the Reynolds stress behaviour. Therefore, the fluctuations of both the spanwise and the wall-normal velocity components are mostly from the small scales, whereas, the fluctuations of the streamwise velocity component is a combination of small scales and large vortices. That is, $\overline{v''^2}$ and $\overline{w''^2}$ are extracted from the mean flow exclusively by the Reynolds stress. Whereas, a global flow oscillation extracts $\overline{u''^2}$ in addition to the Reynolds stress.

Figure 21 (left) illustrates the variation of the maximum $\overline{w''^2}$ with the angle of attack. The plot shows three distinct ranges of angles of attack. For the angles of attack $\alpha < 9.25^\circ$, the maximum value of $\overline{w''^2}$ increases linearly with the angle of attack. In this range of angles of attack, the flow is attached and the LSB is present and intact. The second range of angles of attack is $9.25^\circ \leq \alpha \leq 9.6^\circ$. This is the range where the LSB becomes unstable and the bursting and reformation cycle starts to develop. As seen in the figure, the maximum value of $\overline{w''^2}$ decreases rapidly and linearly as the angle of attack is increased. In the third range, $\alpha \geq 9.7^\circ$, the maximum value of $\overline{w''^2}$ decreases slowly and linearly as the angle of attack is increased. In this range of angles of attack, the bursting and reformation cycle of the LSB becomes fully developed. The variation of the locations of the maximum $\overline{w''^2}$ with the angle of attack is illustrated in figure 21 (right). The locations are closer to the aerofoil surface compared to their $\overline{u''^2}$ and $\overline{v''^2}$ counterparts. The maximum value of $\overline{w''^2}$ moves upstream towards the aerofoil leading-edge until the angle of attack is 9.0° . After that, it moves downstream towards the trailing-edge.

3.4 Reynolds stress

It is well known that it is the Reynolds stress acting against the mean flow shear that extracts energy from the mean and feeds it into the small-scale perturbations. Also, it is well established that the Reynolds stress is proportional to the mean velocity gradient. The velocity gradient in the separated shear layer in the vicinity of the leading-edge and the shear layer at the trailing-edge are very strong. The Reynolds stress generated by the former is negative, and that produced by the latter is positive. Apparently, this is because at the trailing-edge the shear stress tends to create anticlockwise vortices, whereas, at the leading-edge, it tends to generate clockwise vortices. As the angle of attack is increased, the magnitude of the Reynolds stress in the vicinity of the leading-edge increases to a maximum value at 9.2° then it drops almost linearly with the angle of attack. At the trailing-edge, the Reynolds stress increases monotonically with the angle of attack. However, the production of the turbulent kinetic energy does not only depend on the Reynolds stress, but also it depends on the mean shear. Therefore, an increase of the Reynolds stress does not guarantee an increase in the extraction of turbulent kinetic energy from the mean flow.

Figure 22 shows the Reynolds stress distribution for the mean flow-fields. The magnitude of the Reynolds stress is less than that of the high-lift and higher than that of the low-lift. This is consistent, in general, with the above discussion on turbulent kinetic energy in § 3.3. The left-hand side of figure 23 illustrates the distance of the minimum Reynolds stress in x direction, from the aerofoil leading-edge, and in y direction from the aerofoil surface. As seen in the figure, the location of the minimum Reynolds stress moves, in x direction, towards the leading-edge until it reaches the closest point to the leading-edge at the angle of attack of 9.25° . After that, the location of the minimum Reynolds stress moves away from the leading-edge as the angle of attack is increased. The location of minimum Reynolds stress moves away from the aerofoil surface as the angle of attack is increased.

Figure 23 (right) shows that the magnitude of the Reynolds stress reached a maximum at the angle of attack of 9.2° . This angle is a little bit lower than the angle at which $\overline{v''^2}$ and $\overline{w''^2}$ reached their maximum magnitude. The difference in the angle of attack of 0.05° can be considered within statistical error. However, the angle of minimum Reynolds stress is much lower than that of maximum $\overline{u''^2}$ which is 9.4° . This implies that the perturbations of the wall-normal and the spanwise velocity components are extracted from the mean flow exclusively by the Reynolds stress. Whereas, a global flow oscillation generates perturbations in the streamwise velocity in addition to the Reynolds stress.

3.5 Pressure fluctuations

The variance of the pressure fluctuations is shown in figure 24. As seen in the figure, at $\alpha = 9.25^\circ$, $\overline{p''^2}$ has a significant magnitude around the location of the maximum LSB height and vanishes elsewhere. As the angle of attack is increased, $\overline{p''^2}$ extends downstream the bubble but away from the aerofoil surface in a fashion similar to that observed in $\overline{v''^2}$. However, $\overline{p''^2}$ has a significant magnitude upstream and in the vicinity of the separation location. In the range of angles of attack $9.4^\circ < \alpha < 10.5^\circ$ the pressure fluctuations intensifies in the region between the leading-edge and the LSB. This is indicative that an inflectional inviscid type instability is in action in this region. The variance of the pressure fluctuations for the mean attached flow and the mean separated flow are shown in figures 25 and 26, respectively. Both of $\widehat{p''^2}$ and $\widetilde{p''^2}$ are similar to their mean counterpart; however, they vanish upstream the LSB. At the trailing-edge, the pressure fluctuations significantly intensifies in the statistically separated flow as seen in figure 26.

The profile of the maximum $\overline{p''^2}$ mimics that of $\overline{u''^2}$ but peaks at a lower angle of attack of 9.25° , as seen in the left side of figure 27. In this regards, $\overline{p''^2}$ behaviour is in agreement with that of $\overline{v''^2}$, $\overline{w''^2}$, and $\overline{u''v''}$ except for the pressure fluctuations upstream the LSB.

3.6 Aerodynamic coefficients

The locally-time-averaged pressure coefficient, $\overline{C_p}$, is shown in the left side of figure 28. Ten profiles covering the range of angles of attack 9.25° – 10.5° are presented in the figure. The zoom in window illustrates the distribution of $\overline{C_p}$ in the vicinity of the trailing-edge in the range $0.6 \leq x/c \leq 1.0$. The flow is fully attached at 9.25° , in the mean sense, and fully separated at 10.5° as seen in figures 6, 7, and 9. Near the aerofoil leading-edge, a laminar boundary layer develops, and the pressure coefficient decreases drastically. The boundary layer remains laminar until the pressure gradient changes from favourable to adverse. Consequently, the laminar boundary layer detaches and travels away from the aerofoil surface to create a region of separated flow near the surface. The flow then reattaches to the aerofoil surface, and an LSB is formed. The pressure gradient seems to be favourable across the bubble in the range $0.05 < x/c < 0.3$. Downstream the bubble the pressure gradient becomes adverse, but the flow has enough momentum to overcome separation. Further downstream, the pressure coefficient remains almost constant. As a consequence of the bubble bursting, the pressure coefficient gradually diminishes in magnitude and flattens at higher angles of attack. At the vicinity of the trailing-edge the pressure gradient on the pressure surface of the aerofoil is adverse at 9.25° . As the angle of attack is increased, the pressure distribution becomes favourable as seen on the left-hand side of figure 28. It is noted that at the trailing-edge the pressure distribution shifts upwards gradually as the angle of attack is increased. The pressure coefficient is duly integrated about the aerofoil at each time-step for each angle of attack. The integrated effect of the bubble bursting on the pressure coefficient indeed shows up in the aerodynamic forces, as discussed later.

The locally-time-averaged skin-friction coefficient $\overline{C_f}$ in the same range of angles of attack is shown in the right side of figure 28. In the vicinity of the leading-edge, the velocity tends to increase rapidly. Hence, a

relatively high velocity gradient takes place, and the skin-friction is consequently at maximum values at all of the investigated angles of attack. This is followed by a sharp and sudden drop in the skin-friction until it crosses the x -axis because of the APG and flow separation. The skin-friction becomes positive again around $x/c = 0.2$; this is the region where the *secondary vortex* is formed. The friction coefficient then decreases again and becomes negative before it switches signs again at a location that is dependent on the angle of attack as seen in the figure. In the region of negative \overline{C}_f , the LSB is formed at each angle of attack. At higher angles of attack, the locations where \overline{C}_f switches signs moves further downstream as the mean bubble length increases with the angle of attack. On the suction surface of the aerofoil and in the vicinity of the trailing-edge, \overline{C}_f becomes negative again as a consequence of the TEB. On the pressure surface, however, \overline{C}_f increases in the vicinity of the trailing-edge as the angle of attack is increased.

The left-hand side (top) of figure 29 illustrates the averaged values of C_L for all of the investigated angles of attack. The circles denote the mean time-averaged lift coefficient, \overline{C}_L ; the upward triangles display the high-lift time-averaged lift coefficient, \widehat{C}_L ; and the downward triangles denote the low-lift time-averaged lift coefficient, \widetilde{C}_L . The values of C_L reaches its maximum at $\alpha = 9.0^\circ$ and decreases with the angle of attack down to $\alpha = 9.3^\circ$. A drastic and abrupt loss of lift then takes place in the range of angles of attack $9.3^\circ < \alpha < 9.8^\circ$. After that, the lift resumes decreasing almost linearly but faster than that observed in the range of $\alpha = 9.0^\circ - 9.3^\circ$.

The solid line with filled black squares denotes the experimental data of Ohtake *et al.* (2007) at $Re_c = 5 \times 10^4$ transformed to its corresponding compressible counterpart using the Prandtl–Glauert rule Glauert (1928). The filled black circles denote the LES data by Almutairi & Alqadi (2013). The Prandtl–Glauert rule applies to potential flows at small angles of attack; however, it gives an estimate of how the incompressible experimental data of Ohtake *et al.* (2007) and its corresponding compressible data transformed with the Prandtl–Glauert rule compare to the compressible LES data at $M_\infty = 0.4$. Subsonic and incompressible potential flows have zero drag. Therefore, only C_L was transformed with the Prandtl–Glauert rule. The effect of compressibility can be expressed by the shift in the coefficient magnitude and the angle of attack at which the coefficients have maximum values. The lift coefficient compares very well to that of the LES data by Almutairi & Alqadi (2013). However, Almutairi & Alqadi (2013) used a coarser grid (Grid-1) compared to the grid resolution used in the present study. Hence, the systematic and consistent shift in the magnitude of C_L .

The right-hand side (top) of figure 29 shows the averaged values of C_D for all of the investigated angles of attack. The circles denote the mean drag coefficient, \overline{C}_D ; the upward triangles display the high-lift drag coefficient, \widehat{C}_D ; the downward triangles denote the low-lift drag coefficient, \widetilde{C}_D ; and the solid line with filled black squares denotes the experimental data of Ohtake *et al.* (2007). The drag coefficient increases slowly and almost linearly in the range of $\alpha = 9.0^\circ - 9.3^\circ$. A sudden increase in the drag takes place in the range $9.3^\circ < \alpha < 9.7^\circ$. After that, it increases slowly with some degree of nonlinearity.

The lift and drag coefficients agree very well qualitatively and with acceptable accuracy quantitatively when compared to that of Ohtake *et al.* (2007). The relatively small disparity between the LES data and that of the experiment is due to the fact that experimental data are sampled for relatively longer sampling time compared to that of the numerical simulation, hence, the convergence of the statistics of the experimental data to their true mean is much better than that of the LES statistics.

Figure 29 (bottom-left) displays the averaged values of \overline{C}_m , \widehat{C}_m , and \widetilde{C}_m for all of the investigated angles of attack. As seen in the figure, the moment coefficient mimics the behaviour of the lift coefficient. Figure 29 (bottom-right) shows the averaged values of \overline{C}_f , \widehat{C}_f , and \widetilde{C}_f for all angles of attack. The skin-friction remains almost constant for angles of attack lower than 9.0° . After that, C_f drops linearly in the range $9.0^\circ < \alpha < 9.6^\circ$. Finally, the skin-friction fluctuates around a constant value for the angles of attack $\alpha \geq 9.6^\circ$. It is interesting to note that the difference between \widehat{C}_f and \widetilde{C}_f remains almost constant for all of the angles of attack. It is also noted that the difference between the mean time-averaged skin-friction coefficient and the low-lift time-averaged coefficient remains constant. Unlike C_L , C_D , and C_m where these differences start small at low angles of attack and tend to increase as the angle of attack is increased.

3.7 The lift and the skin-friction spectra

Most of the variations in the pressure field are integrated into the lift coefficient signal. Hence, any globally dominant flow feature is reflected by a peak in the spectrum of C_L . The spectra of the lift coefficient were dully calculated using the fast Fourier transform (FFT) algorithm. For each of the sixteen angles of attack,

the spectrum is dominated by low-frequency peak as seen in figure 30. The C_L spectra peak at low-frequency with a significant amplitude at the angles of attack of $\alpha > 9.5^\circ$. That is, the low-frequency modes gain considerable momentum at the middle of the LFO transition process. The LFO continues to develop and gains more strength until the amplitude reaches a maximum at $\alpha = 9.9^\circ$. It is noted that in most of C_L spectrum there are two peaks at low frequencies. Each peak features a low-frequency flow mode. The two low-frequency modes interact with each other in a manner that relaxes the flow into equilibrium. The spectra of the skin-friction coefficient were calculated similarly. The spectra is similar to that of the lift coefficient as seen in figure 31.

Figure 32 (left) shows the Strouhal number of the most dominant low-frequency oscillations, St , plotted versus the angle of attack for the lift coefficient. Strouhal number decreases very fast and linearly with the angle of attack in the range of $\alpha = 9.0^\circ$ – 9.5° . After that, the Strouhal number increases with the angle of attack. The \times 's denote the non-dimensional frequency f . The filled black circles denote the LES data by Almutairi & Alqadi (2013). However, the Strouhal number increases much faster with the angle of attack in the case of the LES data by Almutairi & Alqadi (2013). This is because they used a coarser grid and consequently overestimated the size of the bubble and the rate at which the kinetic energy dissipated as discussed before. Therefore, the aerofoil in their case undergoes an early full stall at the angle of attack of 9.6° . The Strouhal number of the LFO for the skin-friction coefficient mimics that of the lift coefficient as illustrated in the right-hand side of figure 32.

Time histories of C_L shows no apparent low-frequency oscillations for the angles of attack $\alpha \leq 9.25^\circ$. However, the spectral analysis identified a low-frequency mode at these angles. The low-frequency mode at the angles of attack $\alpha \leq 9.25^\circ$ may feature bubble shedding rather than bubble bursting and reformation. Whereas, the low-frequency mode at angles of attack $\alpha > 9.25^\circ$ features switching between fully attached and fully separated flows as a consequence of bubble bursting and reformation.

Conclusions

The effects of the angle of attack on the characteristics of the laminar separation bubble (LSB), its associated low-frequency flow oscillation (LFO) around a NACA-0012 aerofoil at $Re_c = 5 \times 10^4$ and $M_\infty = 0.4$ was studied. In the range of the investigated angles of attack, statistics of the flow-field suggest the existence of three distinct angle-of-attack regimes:

1. The flow-field and aerodynamic characteristics are not much affected by the LFO for the angles of attack $\alpha < 9.25^\circ$.
2. The flow-field undergoes a transition regime in which the bubble bursting and reformation cycle, LFO, develops until it reaches a quasi-periodic switching between separated and attached flow in the range of angles of attack $9.25^\circ \leq \alpha \leq 9.6^\circ$.
3. The flow-field and aerodynamic characteristics are overwhelmed by a quasi-periodic and self-sustained LFO until the aerofoil approaches the angle of a full stall for the angles of attack $\alpha > 9.6^\circ$.

A trailing-edge bubble (TEB) forms at $\alpha > 9.25^\circ$ and grows with the angle of attack. The LSB and TEB merge and continue to deform until they form an open bubble at $\alpha = 10.5^\circ$. On the suction surface of the aerofoil, the pressure distribution shows that the presence of the LSB induces a gradual and continues adverse pressure gradient (APG) when the flow is attached. The bursting of the bubble causes a gradual and continues favourable pressure gradient (FPG) when the flow is separated. This is indicative that a natural forcing mechanism keeps the flow attached against the APG and separated despite the FPG. The length of the bubble, in the mean sense, decreases to a minimum size of 33.5% of the aerofoil chord at $\alpha = 9.0^\circ$ then it grows in size when the angle of attack is further increased. The maximum reversed velocity (MRV) increases to a maximum of 35.6% of the free-stream velocity and 22% of the local free-stream velocity at $\alpha = 9.0^\circ$ then it decreases as the angle of attack increases. The location of the MRV is closest to the aerofoil leading-edge at the angle of attack of 9.0° .

The variance of the pressure fluctuations, the wall-normal velocity fluctuations, and the spanwise velocity fluctuations have a maximum at the angle of attack of 9.25° . The Reynolds stress has a minimum at the angle of attack of 9.2° , and the variance of the streamwise velocity fluctuations has a maximum of 21% of the free-stream velocity at the angle of attack of 9.4° . It is shown that perturbations of the wall-normal and the spanwise velocity components are extracted exclusively by the local velocity gradient inside the shear

layer via the Kelvin–Helmholtz instability. Whereas, the fluctuations in the streamwise velocity component and the pressure are due to a global oscillation in the flow-field in addition to the velocity gradient across the shear layer. The location of maximum values of the variance of the velocity components is closest to the aerofoil leading-edge at the angle of attack of 9.25° or at the inception of the LFO transition regime. The location of the minimum Reynolds stress and the maximum variance of the pressure fluctuations is closest to the aerofoil leading-edge at the angles of attack of 9.0° and 9.5° , respectively. The location of the maximum reversed velocity (MRV), the locations of the maximum variance, and the location of the minimum Reynolds stress move away from the aerofoil surface as the angle of attack increases.

The characterisation parameters are the bubble size; the maximum reversed flow (MRV); the minimum Reynolds stress; the maximum values of the variance of the velocities and the pressure; their distances from the aerofoil leading-edge and from the aerofoil surface; the aerodynamic coefficients; and the Strouhal number of the LFO. In the first regime, the characterisation parameters increases as the angle of attack is increased until they approach saturation values. At the beginning of the second regime, the characterisation parameters drop sharply as the angle of attack increases. In the third regime, the characterisation parameters continue to decrease slowly with the angle of attack. The drag coefficient behaviour is different; it continues to increase in the three regimes. The Strouhal number of the LFO phenomenon drops gradually in the first regime, rapidly in the second regime, and rises slowly in the third regime. However, the flow behaviour becomes more stochastic during the third regime, and the number of samples needed for statistical convergence might be much more than that required for the first two regimes.

It is noted that the secondary bubble exists at the same location when the flow is attached and when it is massively separated. This is indicative that the secondary bubble plays a profound role in the underlying mechanism behind the self-sustained quasi-periodic low-frequency switching between attached and separated flow.

The variance of pressure fluctuations has significant magnitude in the laminar portion of the separated shear layer. This is indicative that the instability that generates and sustains the LFO originates at this location. This challenges the traditional theory that links the instability of the LSB to the separated shear layer with its associated Kelvin–Helmholtz mechanism. The present investigation suggests that most of the observations reported in the literature about the LSB and its associated LFO are neither thresholds nor indicators for the inception of the instability, but rather are consequences of it.

Acknowledgements

All computations were performed on **Aziz Supercomputer** at King Abdulaziz university’s High Performance Computing Center (<http://hpc.kau.edu.sa/>). The authors would like to acknowledge the computer time and technical support provided by the center.

References

- ALAM, M. & SANDHAM, N. D. 2000 Direct numerical simulation of ‘short’ laminar separation bubbles with turbulent reattachment. *Journal of Fluid Mechanics* **410**, 1–28.
- ALFEREZ, N., MARY, I. & LAMBALLAIS, E. 2013 Study of stall development around an airfoil by means of high fidelity large eddy simulation. *Flow, turbulence and combustion* **91** (3), 623–641.
- ALMUTAIRI, J., ALQADI, I. & ELJACK, E. 2015 Large eddy simulation of a naca-0012 airfoil near stall. In *Fröhlich J., Kuerten H., Geurts B., Armenio V. (eds) Direct and Large-Eddy Simulation IX. ERCOFTAC Series, vol 20.*, pp. 389–395. Springer, Cham.
- ALMUTAIRI, J., ELJACK, E. & ALQADI, I. 2017 Dynamics of laminar separation bubble over naca-0012 airfoil near stall conditions. *Aerospace Science and Technology* **68**, 193 – 203.
- ALMUTAIRI, J. H. & ALQADI, I. M. 2013 Large-eddy simulation of natural low-frequency oscillations of separating–reattaching flow near stall conditions. *AIAA journal* **51** (4), 981–991.
- BROEREN, A. P. & BRAGG, M. B. 1999 Flow field measurements over an airfoil during natural low-frequency oscillations near stall. *AIAA journal* **37** (1), 130–132.

-
- BROEREN, A. P. & BRAGG, M. B. 2001 Spanwise variation in the unsteady stalling flowfields of two-dimensional airfoil models. *AIAA journal* **39** (9), 1641–1651.
- CARPENTER, M. H., NORDSTRÖM, J. & GOTTLIEB, D. 1999 A stable and conservative interface treatment of arbitrary spatial accuracy. *Journal of Computational Physics* **148** (2), 341–365.
- ELJACK, ELTAYEB 2017 High-fidelity numerical simulation of the flow field around a naca-0012 aerofoil from the laminar separation bubble to a full stall. *International Journal of Computational Fluid Dynamics* **31** (4-5), 230–245.
- ELJACK, E., ALQADI, I., ALMUTAIRI, J. & SORIA, J. 2016 Large eddy simulation of the low frequency flow oscillation over naca-0012 aerofoil. In *20th Australasian Fluid Mechanics Conference*. Perth, Australia.
- GAITONDE, D. V. & VISBAL, M. R. 1998 *High-order schemes for Navier-Stokes equations: algorithm and implementation into FDL3DI* (No. Air Force Research Lab Wright-Patterson AFB OH Air Vehicles Directorate).
- GASTER, M. 1967 *The structure and behaviour of laminar separation bubbles*. HMSO.
- GLAUERT, H. 1928 The effect of compressibility on the lift of an aerofoil. *Proceedings of the Royal Society of London. Series A, Containing Papers of a Mathematical and Physical Character* **118** (779), 113–119.
- HAMMOND, D. A. & REDEKOPP, L. G. 1998 Local and global instability properties of separation bubbles. *European Journal of Mechanics-B/Fluids* **17** (2), 145–164.
- HORTON, H. P. 1968 Laminar separation bubbles in two and three dimensional incompressible flow. PhD thesis, Queen Mary College.
- INAGAKI, M., KONDOH, T. & NAGANO, Y. 2005 A mixed-time-scale sgs model with fixed model-parameters for practical les. *Journal of fluids engineering* **127** (1), 1–13.
- JONES, LLOYD EDWARD 2008 Numerical studies of the flow around an airfoil at low reynolds number. PhD thesis, University of Southampton.
- JONES, L. E., SANDBERG, R. D. & SANDHAM, N. D. 2010 Stability and receptivity characteristics of a laminar separation bubble on an aerofoil. *Journal of Fluid Mechanics* **648**, 257–296.
- MARXEN, OLAF & HENNINGSON, DAN 2008 Direct numerical simulation of a short laminar separation bubble and early stages of the bursting process. In *New Results in Numerical and Experimental Fluid Mechanics VI*, pp. 235–243. Springer.
- MARXEN, O., YOU, D. & MOIN, P. 2007 Numerical simulations of the bursting of a laminar separation bubble and its relation to airfoil stall. In *Advances in Turbulence XI*, pp. 712–714. Springer.
- MCCULLOUGH, G. B. & GAULT, D. E. 1951 *Examples of three representative types of airfoil-section stall at low speed*. NACA TN 2502.
- MELVILL JONES, B. 1934a *An Experimental Study of the Stalling of Wings*. Air Ministry. Aeronautical Research Committee. Reports and memoranda . Aeronautical Research Committee.
- MELVILL JONES, B. 1934b Stalling. *The Journal of the Royal Aeronautical Society* **38** (285), 753–770.
- MUKAI, JUNICHI, ENOMOTO, SHUNJI & AOYAMA, TAKASHI 2006 Large-eddy simulation of natural low-frequency flow oscillations on an airfoil near stall. *AIAA Paper* **1417**.
- NIU, TAI RAN 1993 The stability of the flow in a laminar separation bubble. *NASA STI/Recon Technical Report N* **95**, 26809.
- OHTAKE, T., NAKAE, Y. & MOTOHASHI, T. 2007 Nonlinearity of the aerodynamic characteristics of naca-0012 aerofoil at low reynolds numbers (in japanese). *Journal of The Japan Society for Aeronautical and Space Sciences* **55** (644), 439–445.

-
- OWEN, P. R. & KLANFER, L. 1953 *On the laminar boundary layer separation from the leading edge of a thin aerofoil*. RAE Rep. Aero. 2508 (Oct. 1953); reissued as A.R.C. CP 220 (1955).
- RINOIE, K. & TAKEMURA, N. 2004 Oscillating behaviour of laminar separation bubble formed on an aerofoil near stall. *Aeronautical Journal* **108** (1081), 153–163.
- SANDBERG, R. D. & SANDHAM, N. D. 2006 Nonreflecting zonal characteristic boundary condition for direct numerical simulation of aerodynamic sound. *AIAA journal* **44** (2), 402–405.
- SANDHAM, N. D. & YEE, H. C. 2001 Entropy splitting for high order numerical simulation of compressible turbulence. In *Computational Fluid Dynamics 2000*, pp. 361–366. Springer.
- SANDHU, H. S. & SANDHAM, N. D. 1994 Boundary conditions for spatially growing compressible shear layers. *Rept. QMW-EP-1100, Faculty of Engineering, Queen Mary and Westfield College, Univ. of London, London* .
- TANAKA, HIROYUKI 2004 Flow visualization and piv measurements of laminar separation bubble oscillating at low frequency on an airfoil near stall. In *International Congress of the Aeronautical Sciences*, pp. 1–15. Yokohama, Japan: International Council of the Aeronautical Sciences, Bonn.
- VREMAN, A. W. 1995 *Direct and large-eddy simulation of the compressible turbulent mixing layer*. University of Twente, Enschede.
- WINKELMAN, A. E. 1990 Flow field studies behind a wing at low reynolds numbers. *AIAA Paper* **1471**, 1–18.
- WINKELMAN, A. E. & BARLOW, J. B. 1980 Flow field model for a rectangular planform wing beyond stall. *AIAA Journal* **18** (8), 1006–1008.
- YON, S. A. & KATZ, J. 1998 Study of the unsteady flow features on a stalled wing. *AIAA journal* **36** (3), 305–312.
- YOUNG, A. D. & HORTON, H. P. 1966 Some results of investigation of separation bubbles. *AGARD Conference Proceedings* **4**, 785–811.
- ZAMAN, K. B. M. Q., MCKINZIE, D. J. & RUMSEY, C. L. 1989 A natural low-frequency oscillation of the flow over an airfoil near stalling conditions. *Journal of Fluid Mechanics* **202**, 403–442.

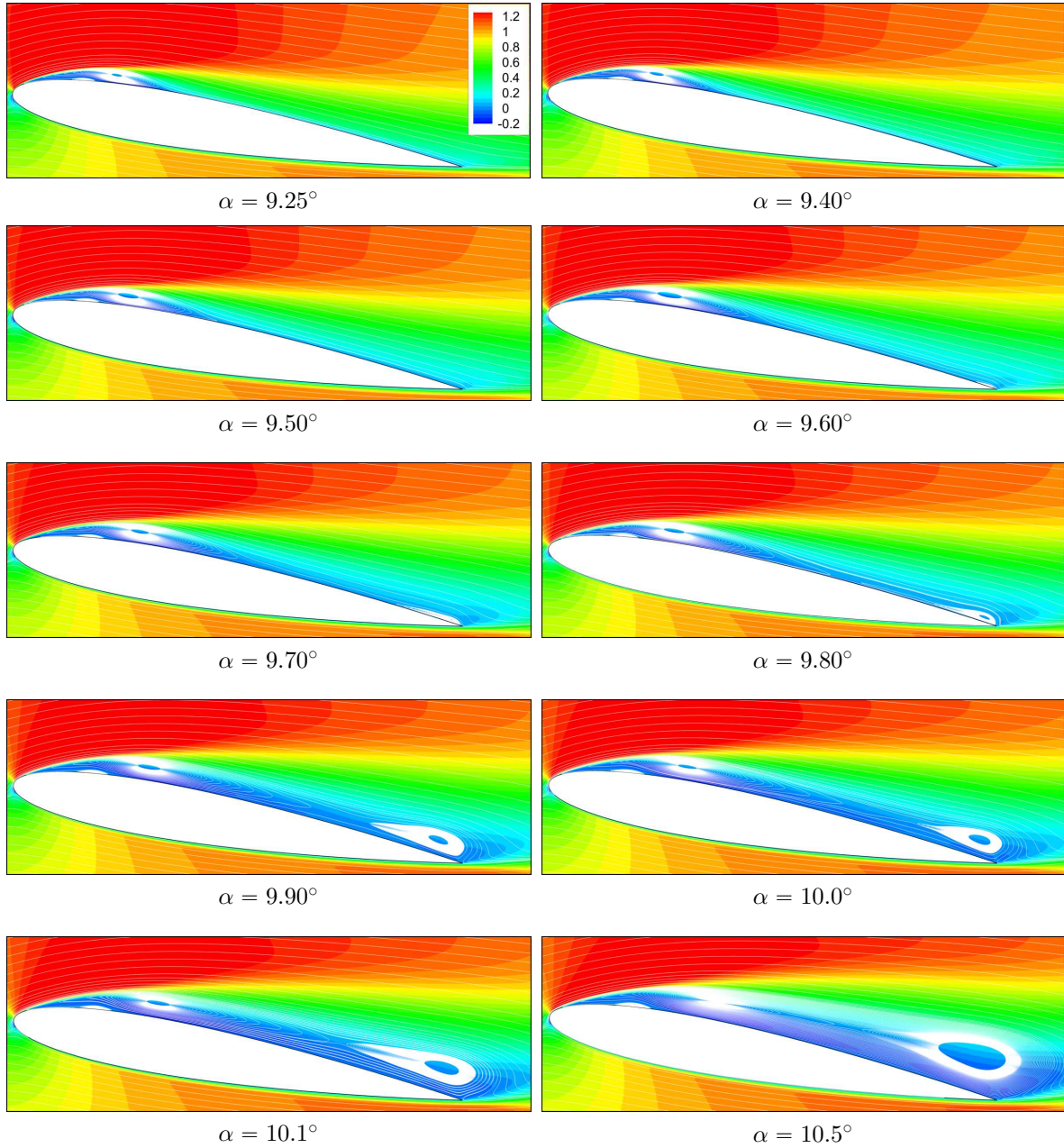


Figure 6. Streamlines patterns of the mean flow-field superimposed on colour maps of the mean streamwise velocity component, \bar{U} , for the angles of attack $\alpha = 9.25^\circ$ – 10.5° .

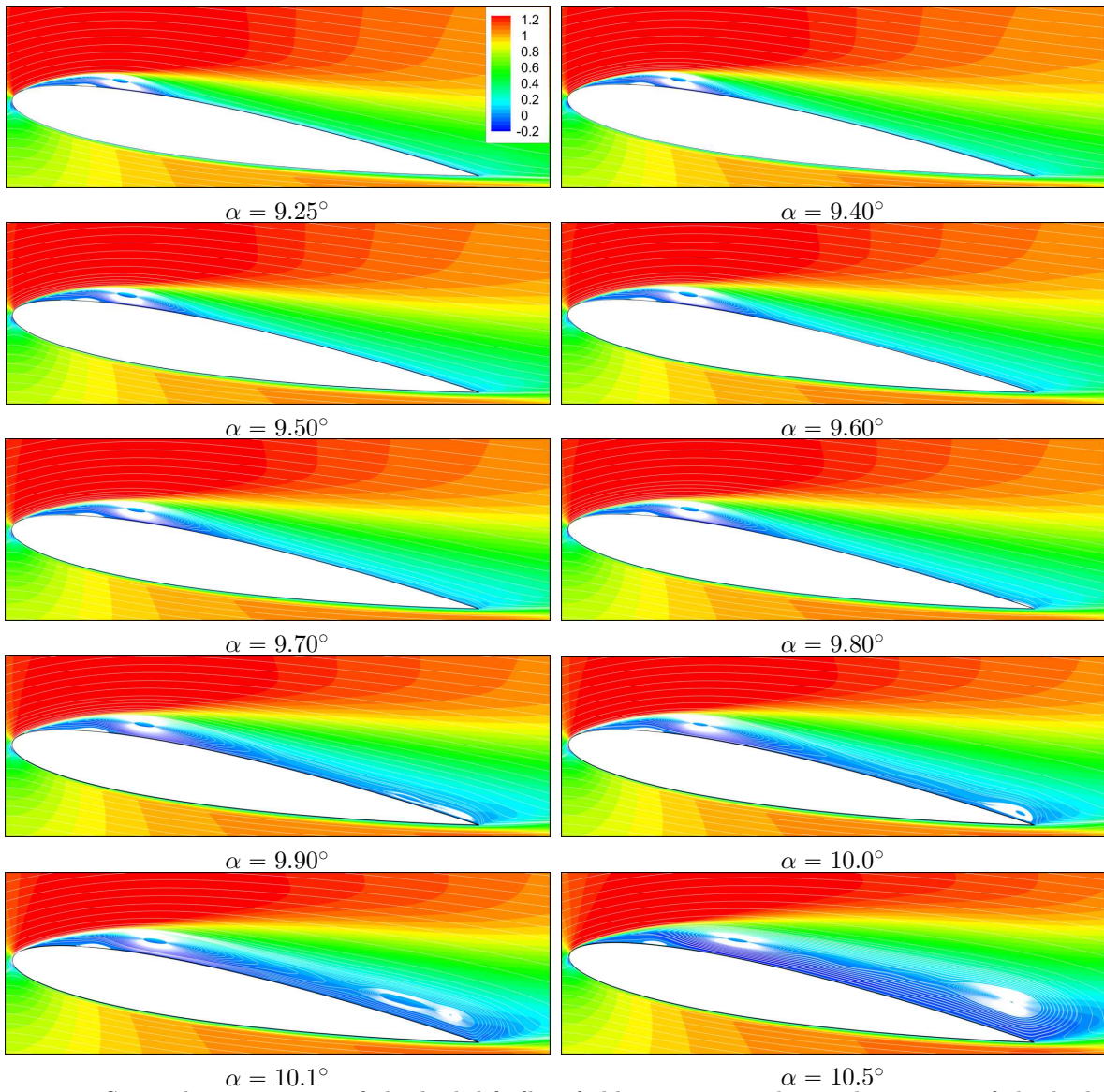


Figure 7. Streamlines patterns of the high-lift flow-field superimposed on colour maps of the high-lift streamwise velocity component, \hat{U} , for the angles of attack $\alpha = 9.25^\circ$ – 10.5° .

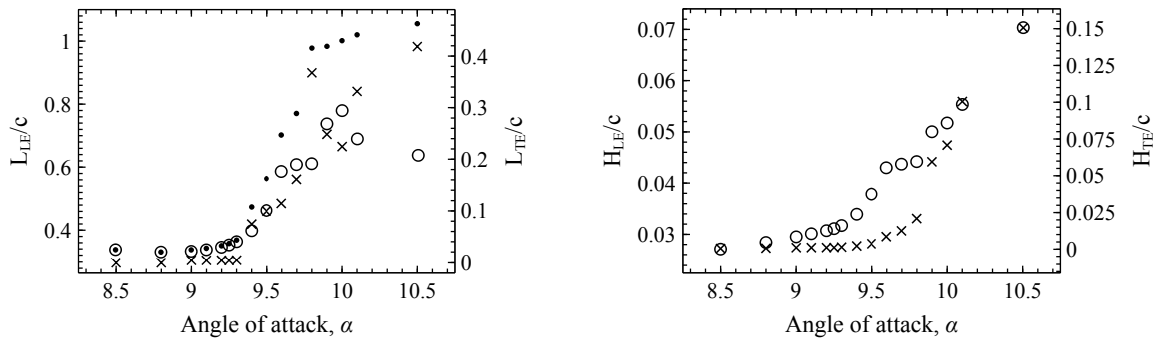


Figure 8. Left: the bubble length plotted versus the angle of attack α . Circles: the length of the leading-edge bubble (L_{LE}); \times 's: the length of the trailing-edge bubble (L_{TE}); black dots: $L_{LE} + L_{TE}$. Right: the bubble height plotted versus the angle of attack α . Circles: the height of the leading-edge bubble (H_{LE}); \times 's: the height of the trailing-edge bubble (H_{TE}).

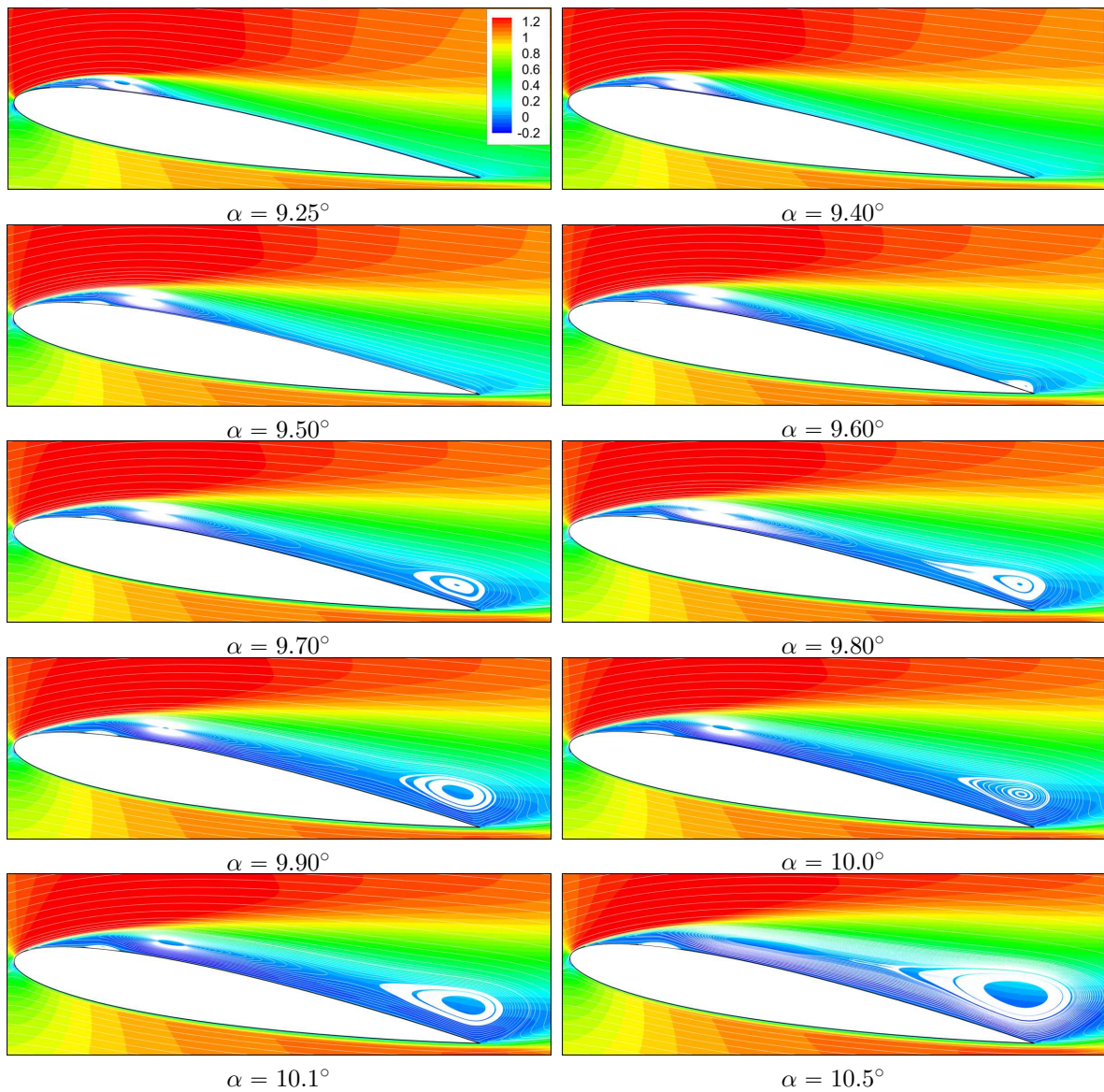


Figure 9. Streamlines patterns of the low-lift flow-field superimposed on colour maps of the low-lift streamwise velocity component, \bar{U} , for the angles of attack $\alpha = 9.25^\circ$ – 10.5° .

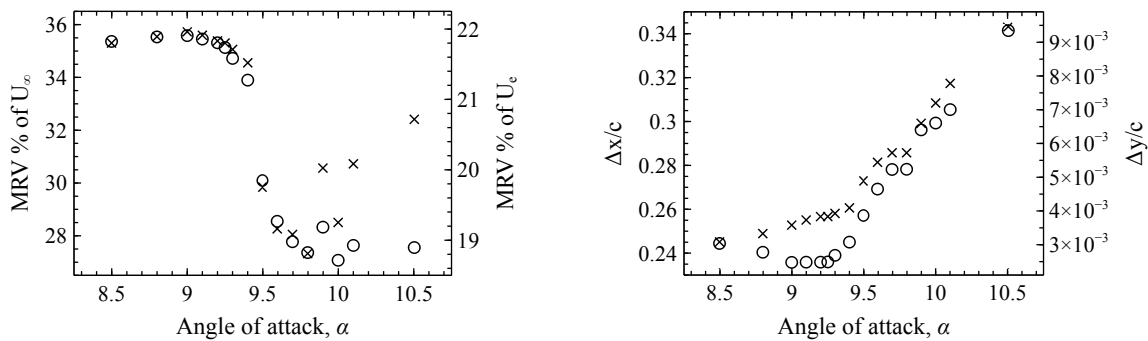


Figure 10. Left: the maximum reverse velocity (MRV) plotted versus the angle of attack α . Circles: the MRV as a percentage of the free-stream velocity U_∞ ; \times 's: the MRV as a percentage of the local free-stream velocity U_e . Right: the location of the MRV plotted versus the angle of attack α . Circles: $\Delta x/c$ measured from the aerofoil leading-edge; \times 's: $\Delta y/c$ measured from the aerofoil surface.

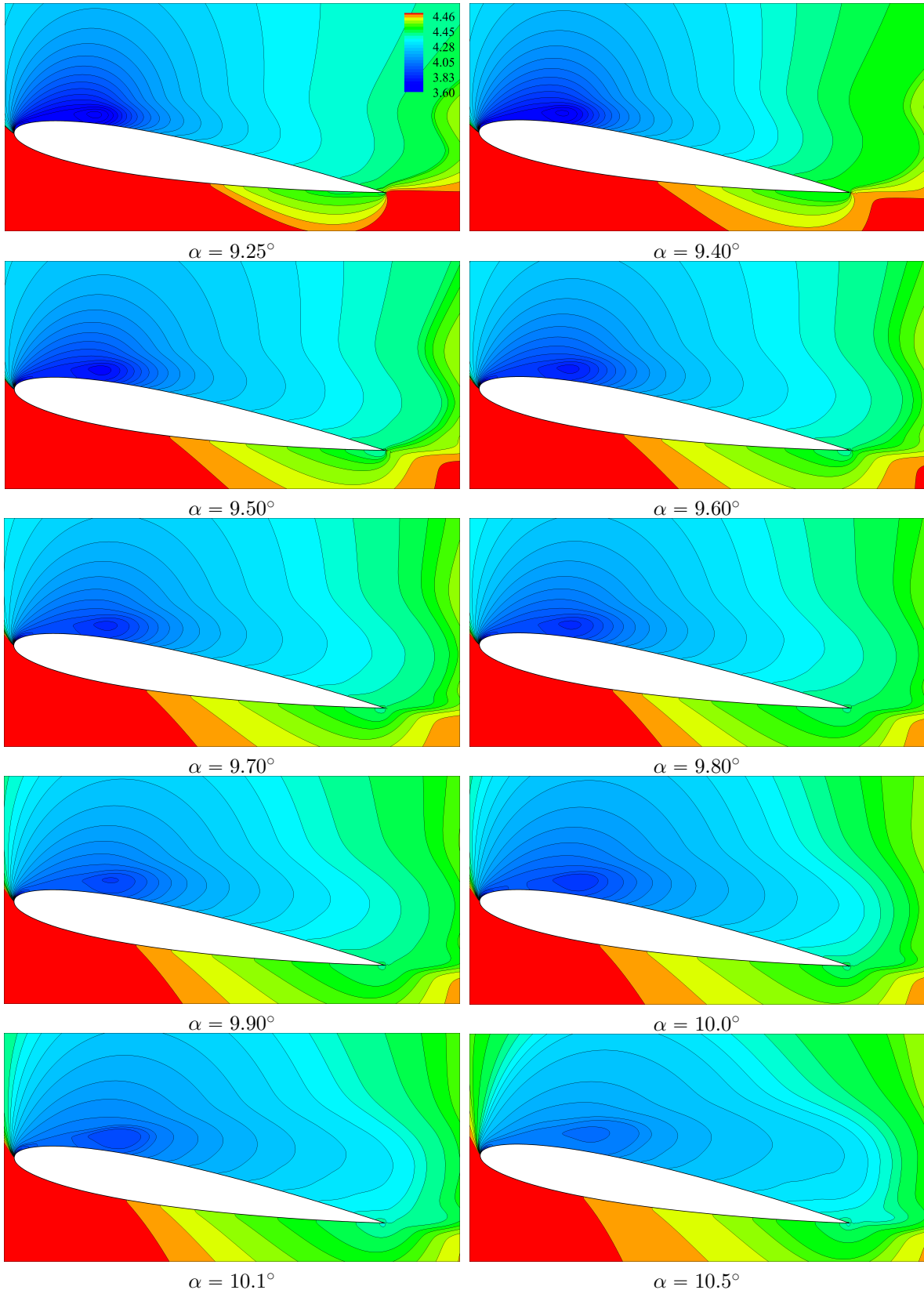


Figure 11. Contours plot of the mean pressure, \bar{P} , for the angles of attack $\alpha = 9.25^\circ$ – 10.5° .

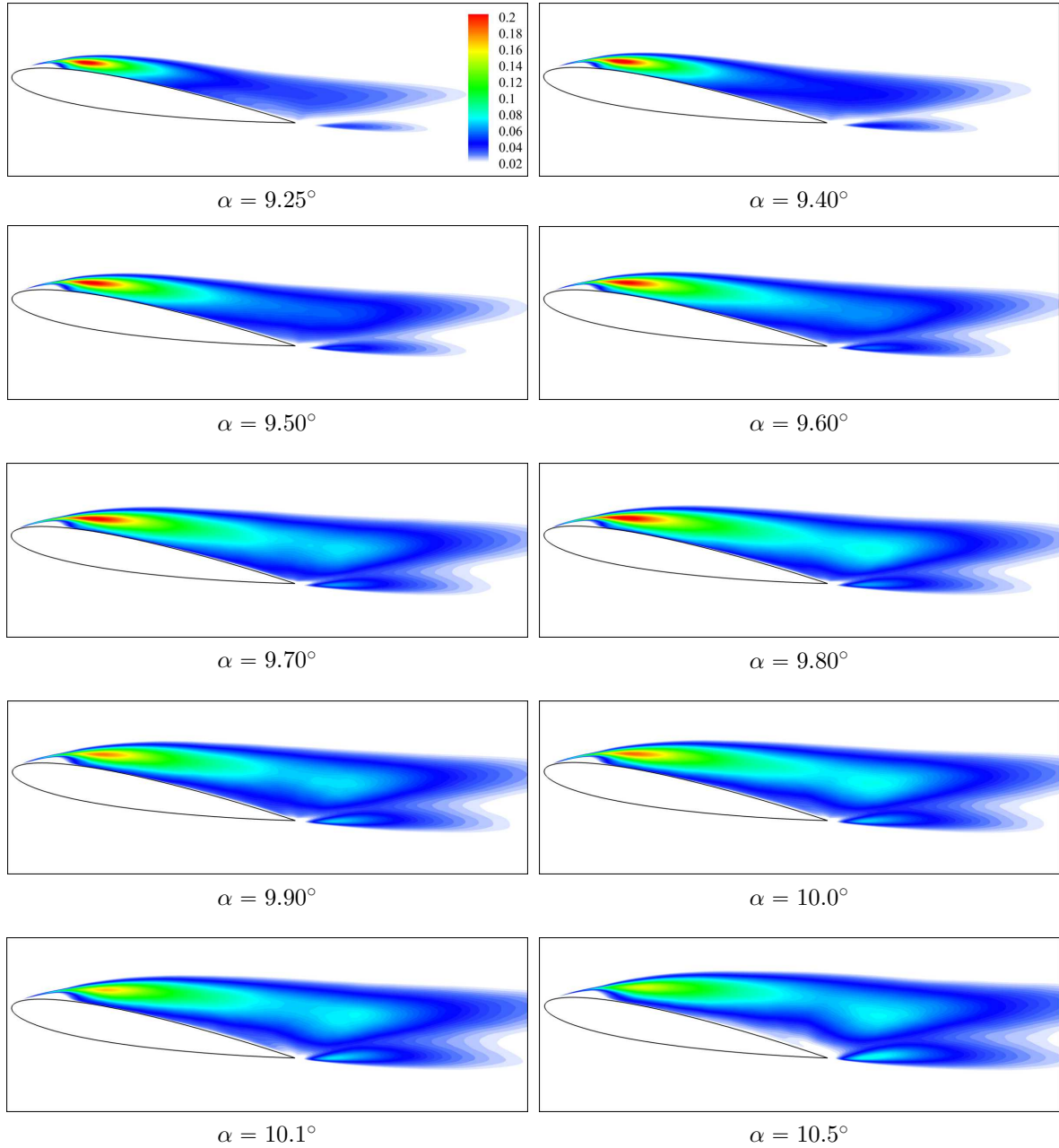


Figure 12. Colours map of the variance of the streamwise velocity component, $\overline{u'^2}$, for the angles of attack $\alpha = 9.25^\circ$ – 10.5° .

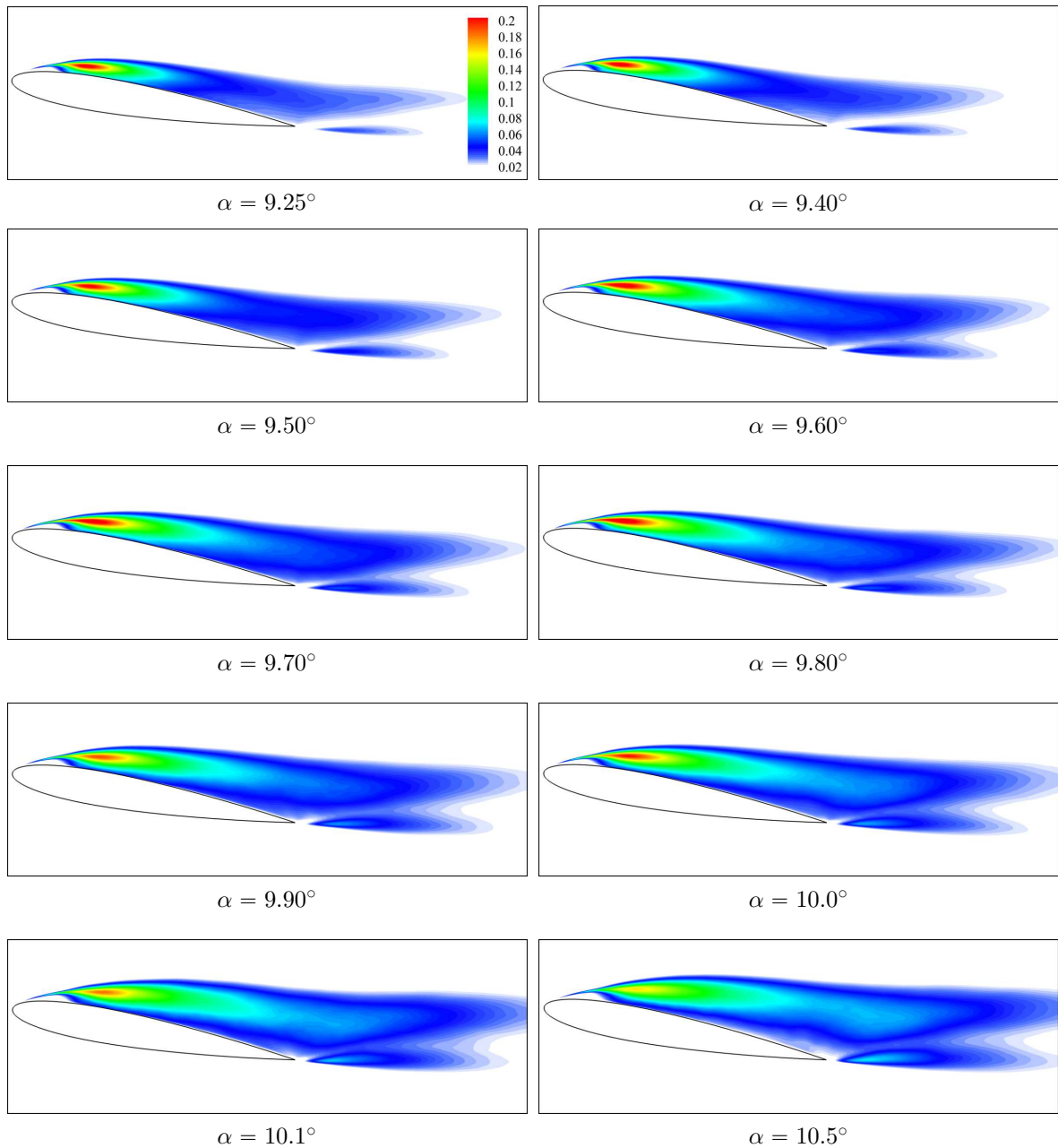


Figure 13. Colours map of the high-lift variance of the streamwise velocity component, $\widehat{u'^2}$, for the angles of attack $\alpha = 9.25^\circ$ – 10.5° .

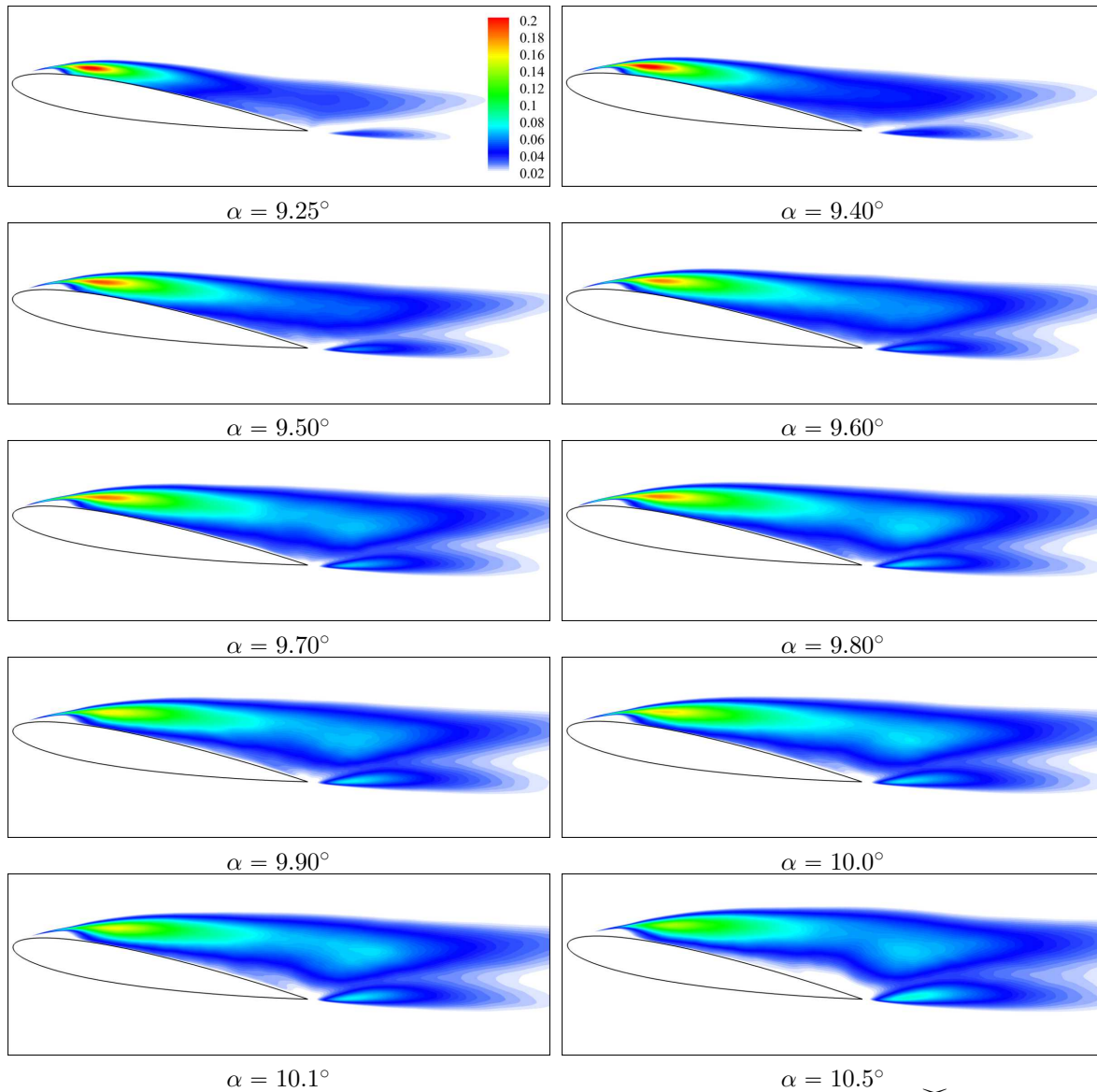


Figure 14. Colours map of the low-lift variance of the streamwise velocity component, $\overline{u''^2}$, for the angles of attack $\alpha = 9.25^\circ$ – 10.5° .

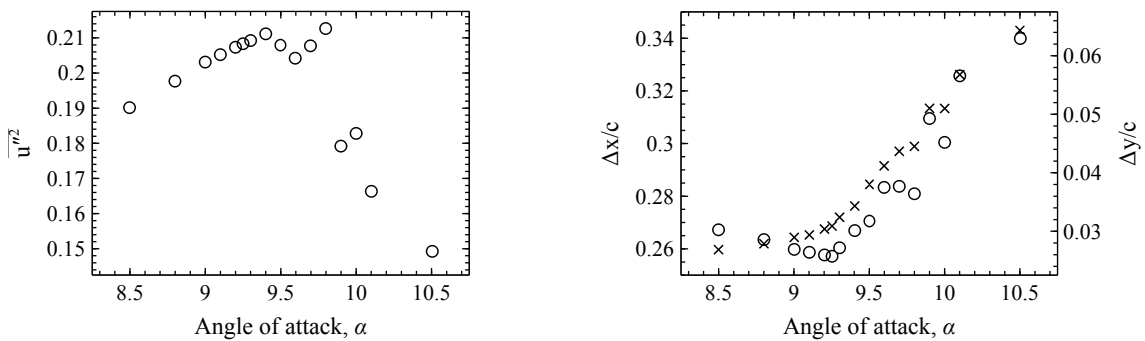


Figure 15. Left: the maximum $\overline{u''^2}$ plotted versus the angle of attack α . Right: the locations of the maximum $\overline{u''^2}$ plotted versus the angle of attack α . Circles: $\Delta x/c$ measured from the aerofoil leading-edge, \times 's: $\Delta y/c$ measured from the aerofoil surface.

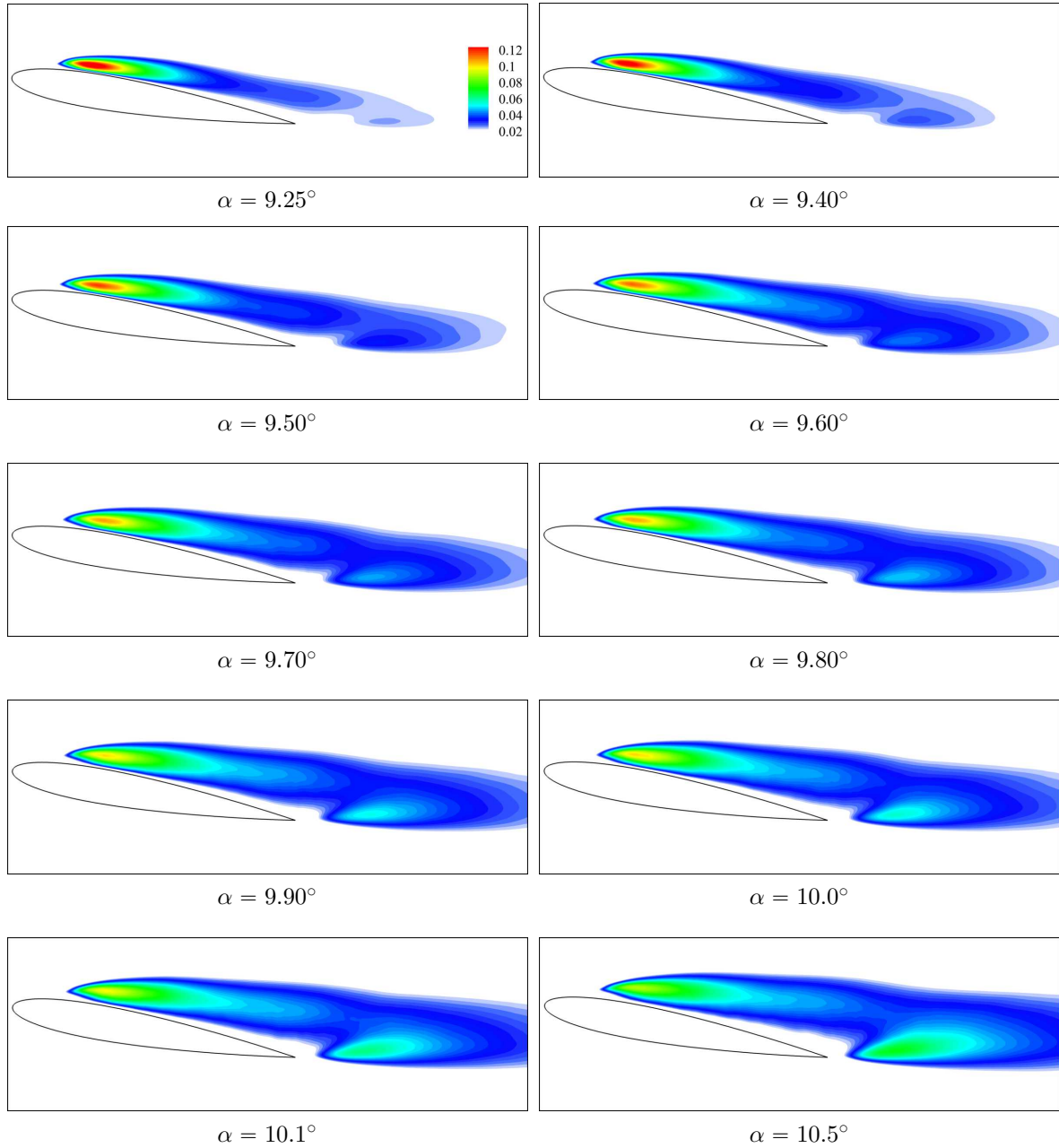


Figure 16. Colours map of the variance of the wall-normal velocity component, $\overline{v''^2}$, for the angles of attack $\alpha = 9.25^\circ$ – 10.5° .

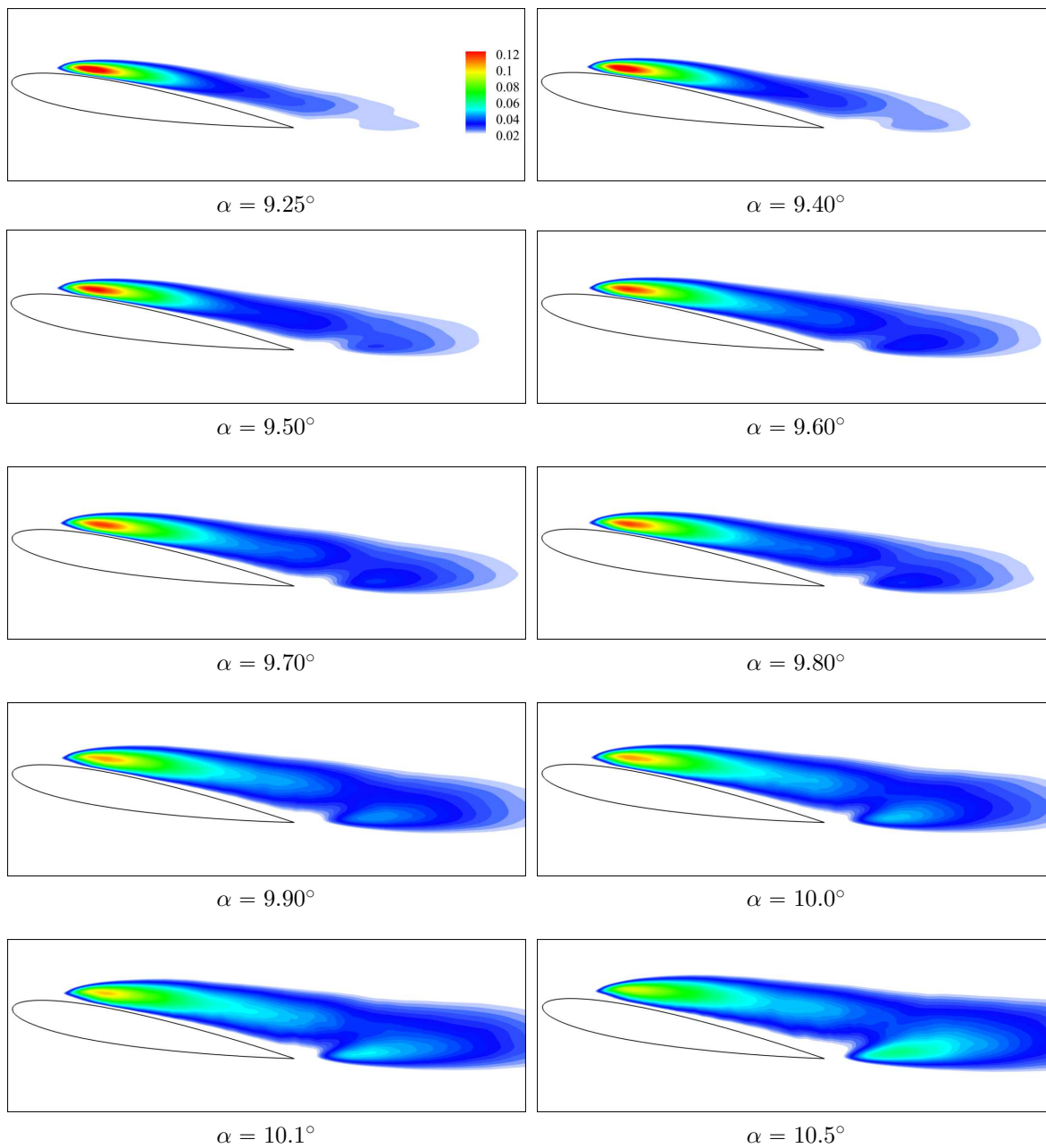


Figure 17. Colours map of the high-lift variance of the wall-normal velocity component, $\widehat{v''^2}$, for the angles of attack $\alpha = 9.25^\circ$ – 10.5° .

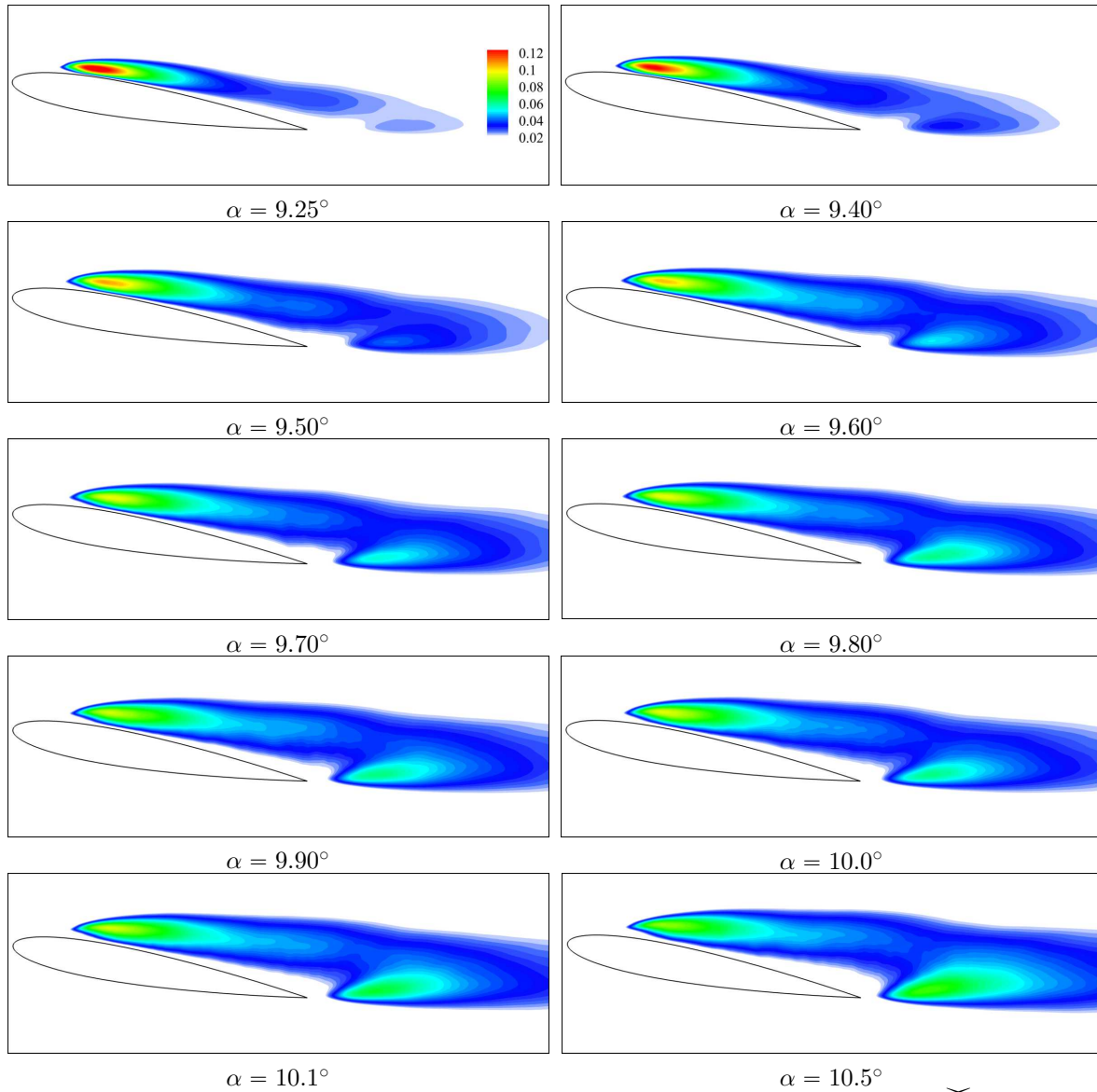


Figure 18. Colours map of the low-lift variance of the wall-normal velocity component, $\overline{v''^2}$, for the angles of attack $\alpha = 9.25^\circ$ – 10.5° .

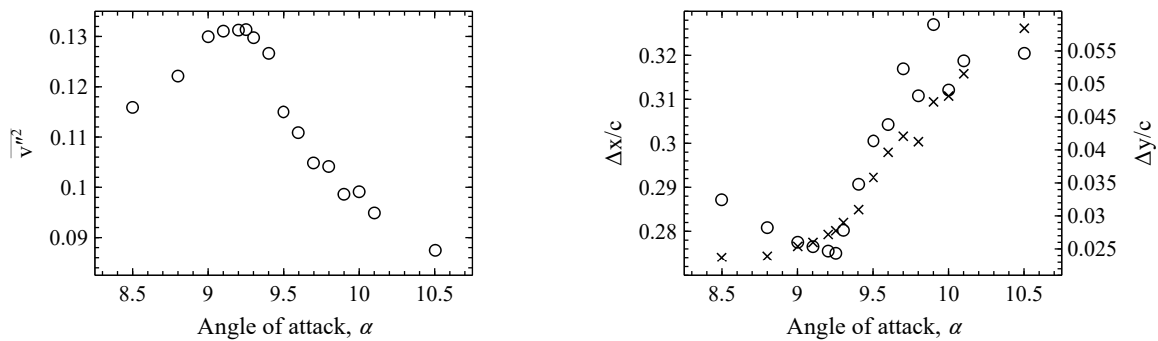


Figure 19. Left: the maximum $\overline{v''^2}$ plotted versus the angle of attack α . Right: the locations of the maximum $\overline{v''^2}$ plotted versus the angle of attack α . Circles: $\Delta x/c$ measured from the aerofoil leading-edge, \times 's: $\Delta y/c$ measured from the aerofoil surface.

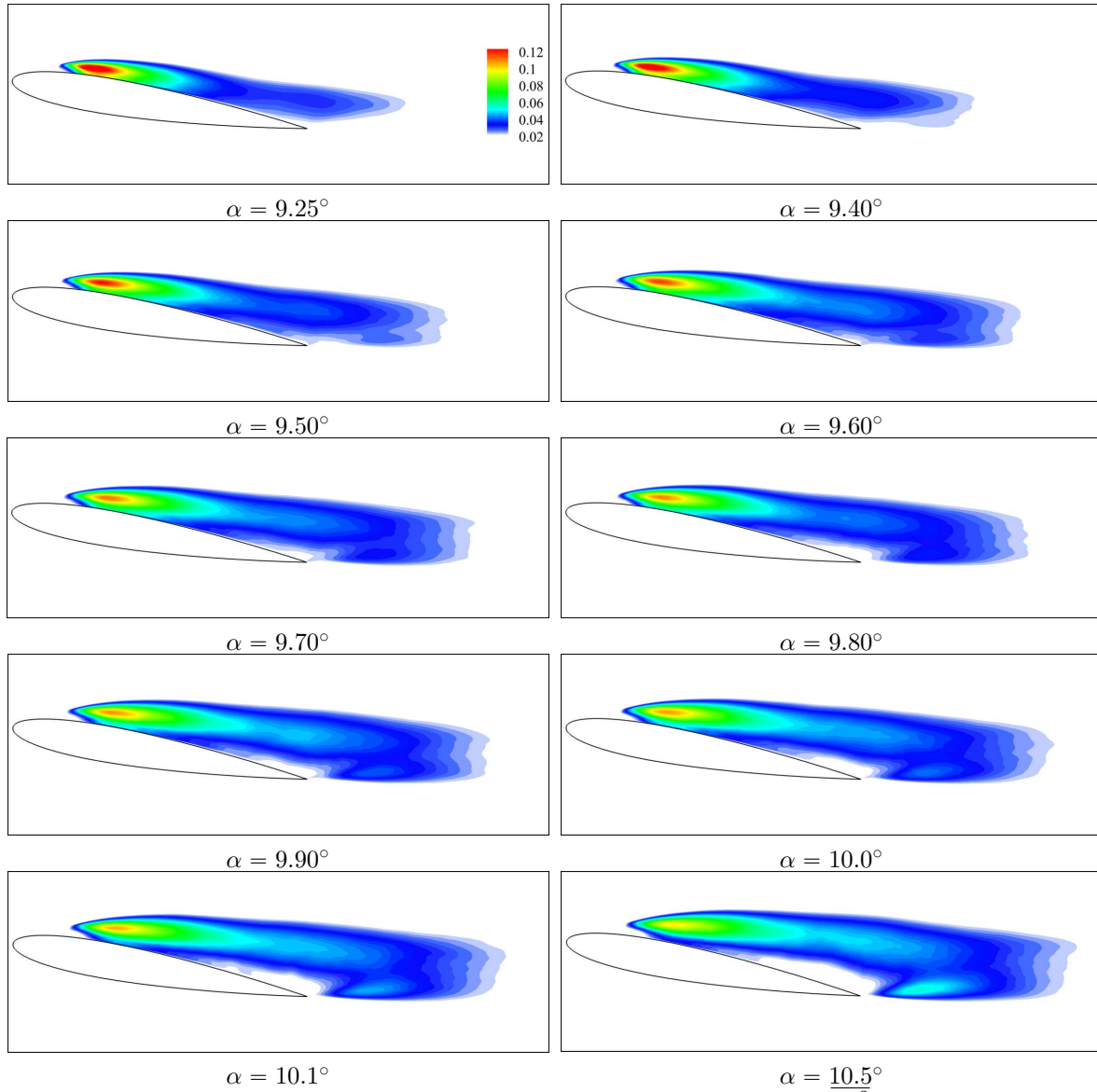


Figure 20. Colours map of the variance of the spanwise velocity component, w''^2 , for the angles of attack $\alpha = 9.25^\circ$ – 10.5° .

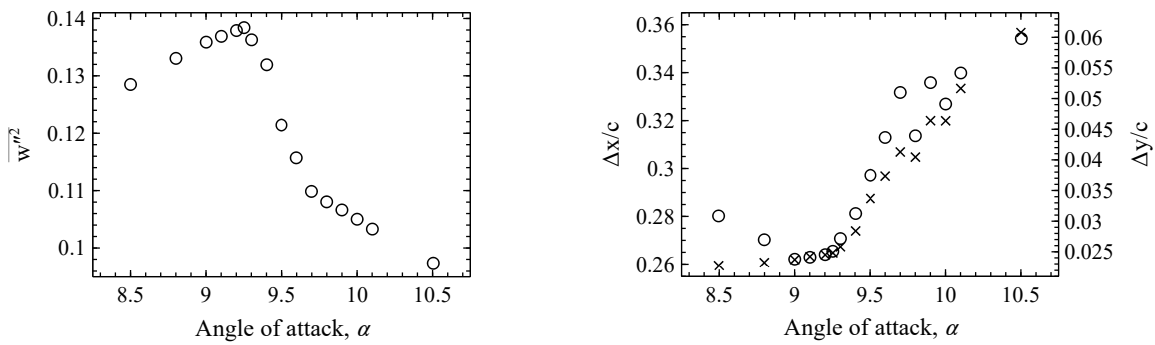


Figure 21. Left: the maximum $\overline{w''^2}$ plotted versus the angle of attack α . Right: the locations of the maximum $\overline{w''^2}$ plotted versus the angle of attack α . Circles: $\Delta x/c$ measured from the aerofoil leading-edge, \times 's: $\Delta y/c$ measured from the aerofoil surface.

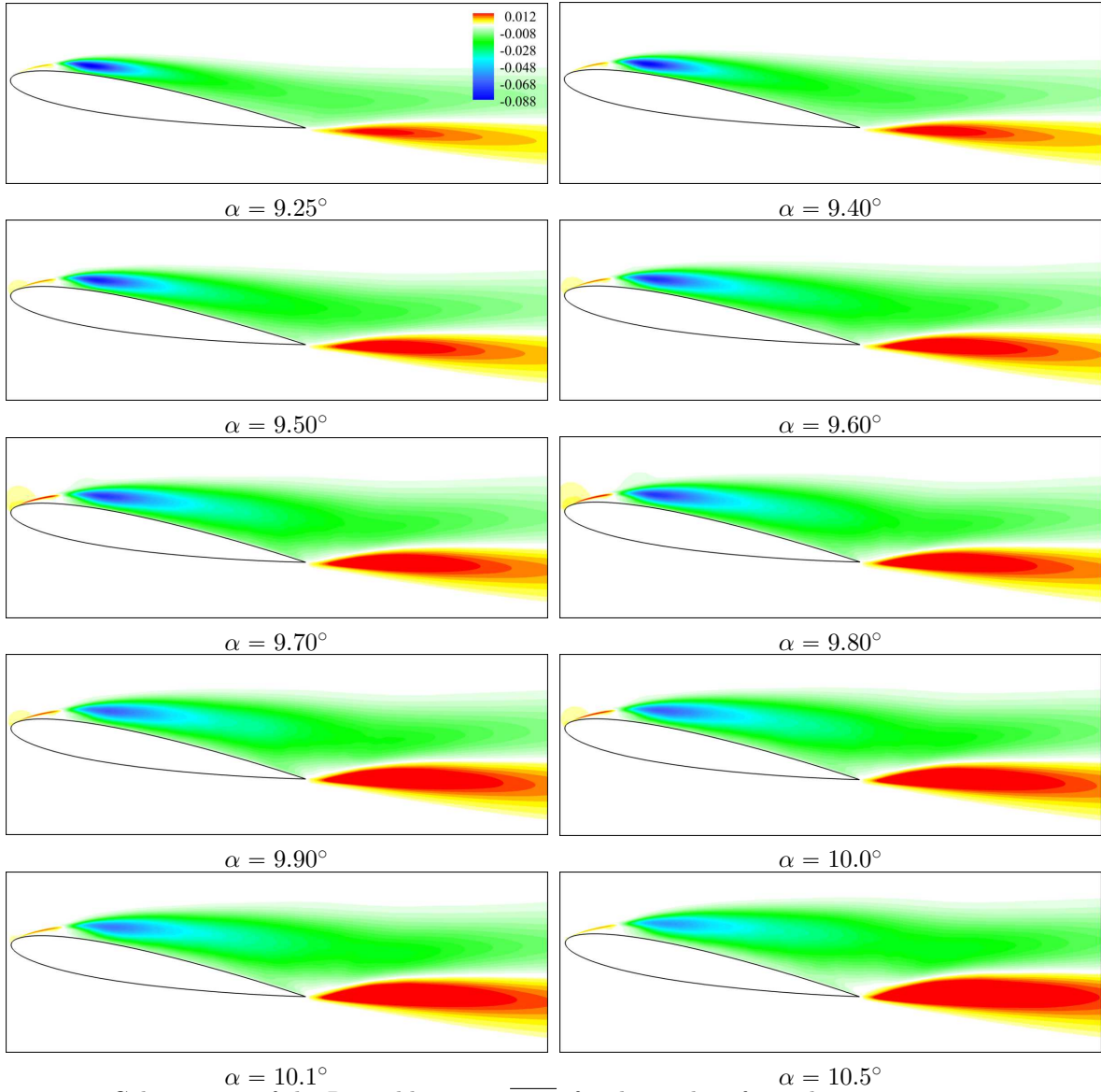


Figure 22. Colours map of the Reynolds stress, $\overline{u''v''}$, for the angles of attack $\alpha = 9.25^\circ$ – 10.5° .

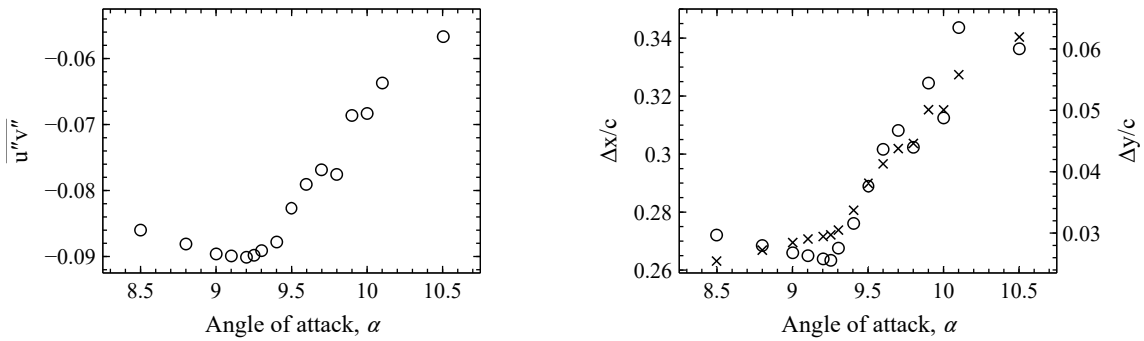


Figure 23. Left: the minimum $\overline{u''v''}$ plotted versus the angle of attack α . Right: the locations of the minimum $\overline{u''v''}$ plotted versus the angle of attack α . Circles: $\Delta x/c$ measured from the aerofoil leading-edge, \times 's: $\Delta y/c$ measured from the aerofoil surface.

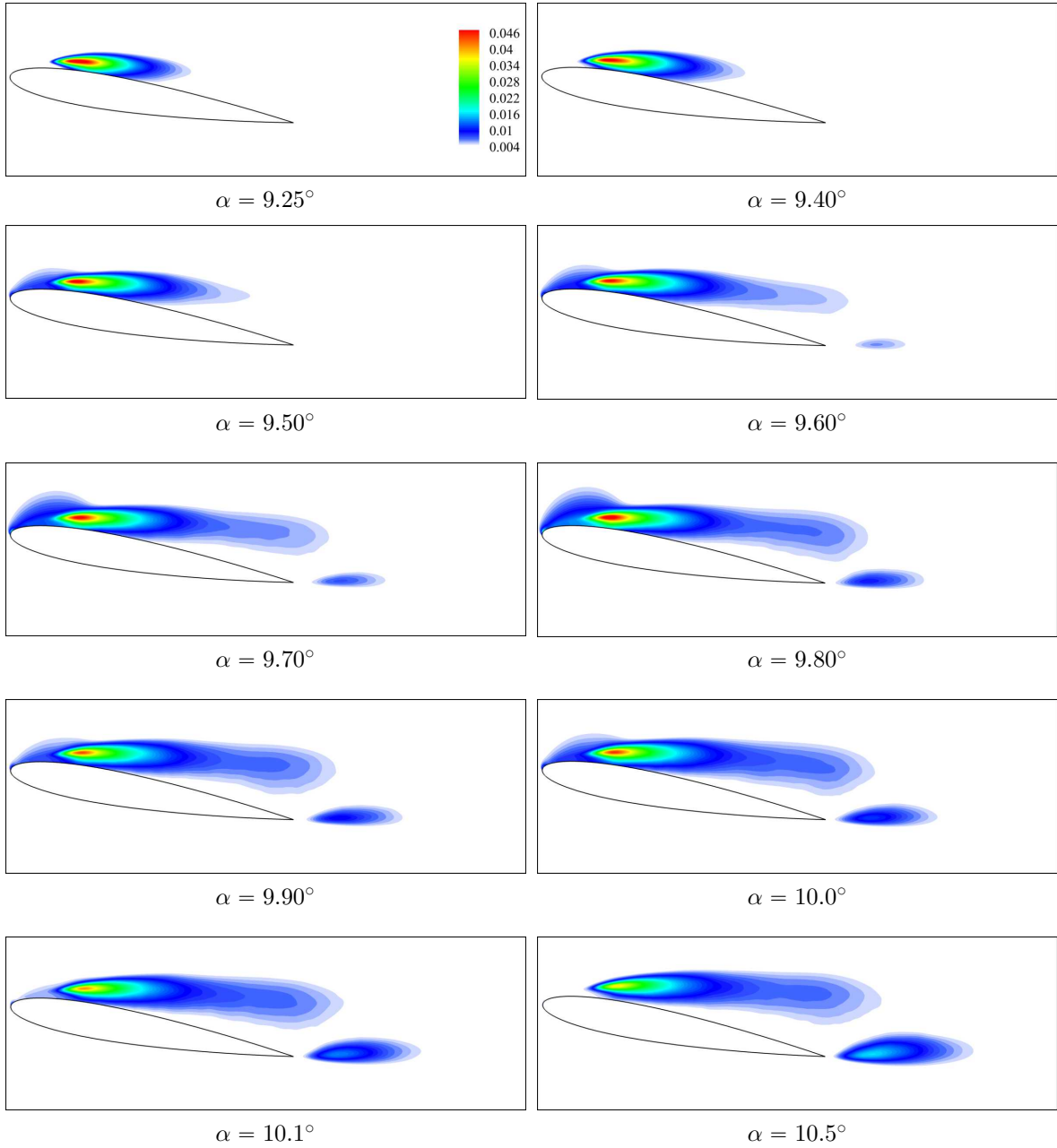


Figure 24. Colours map of the variance of the pressure, $\overline{p''^2}$, for the angles of attack $\alpha = 9.25^\circ$ – 10.5° .

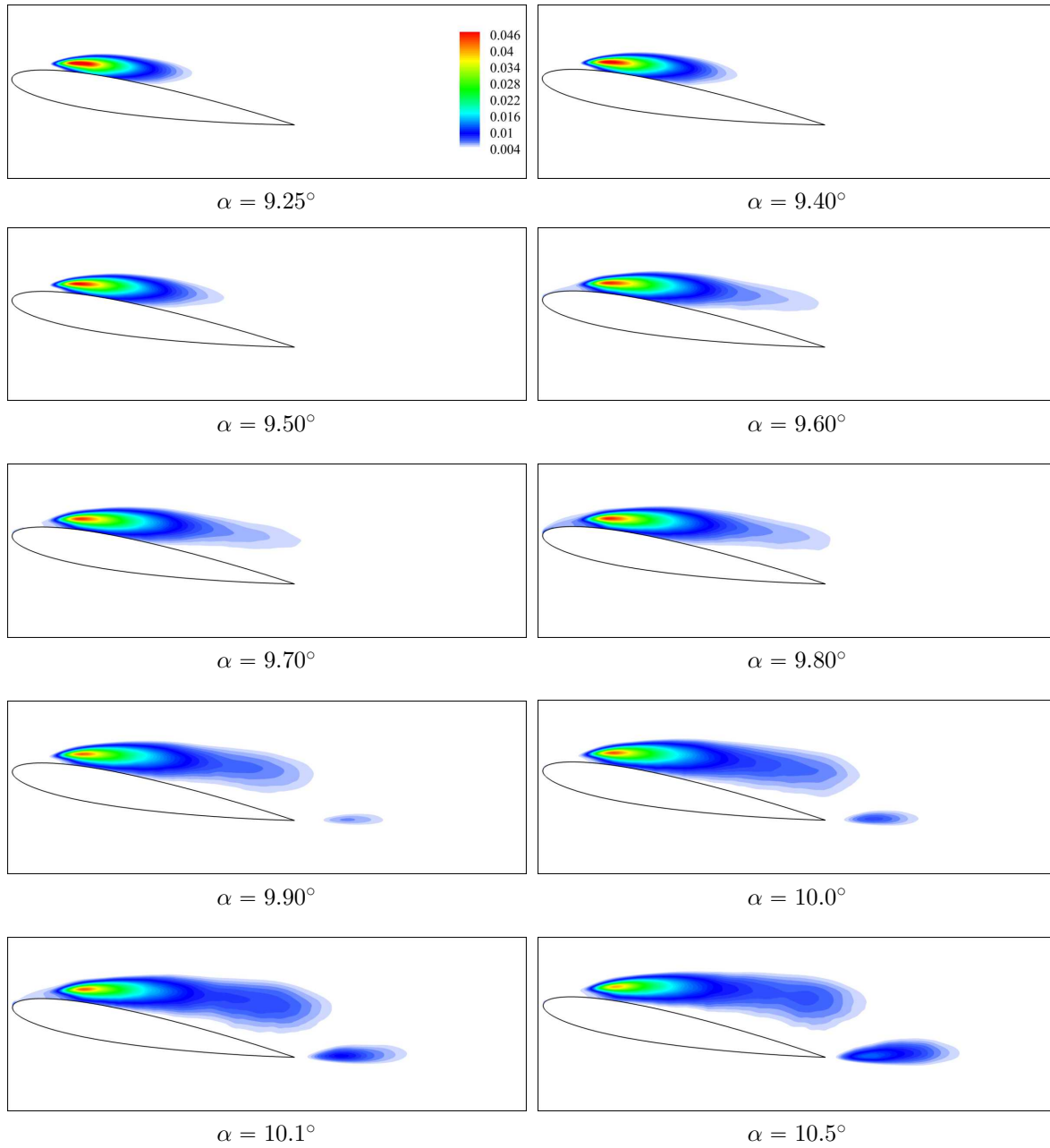


Figure 25. Colours map of the high-lift variance of the pressure, $\widehat{p''^2}$, for the angles of attack $\alpha = 9.25^\circ$ – 10.5° .

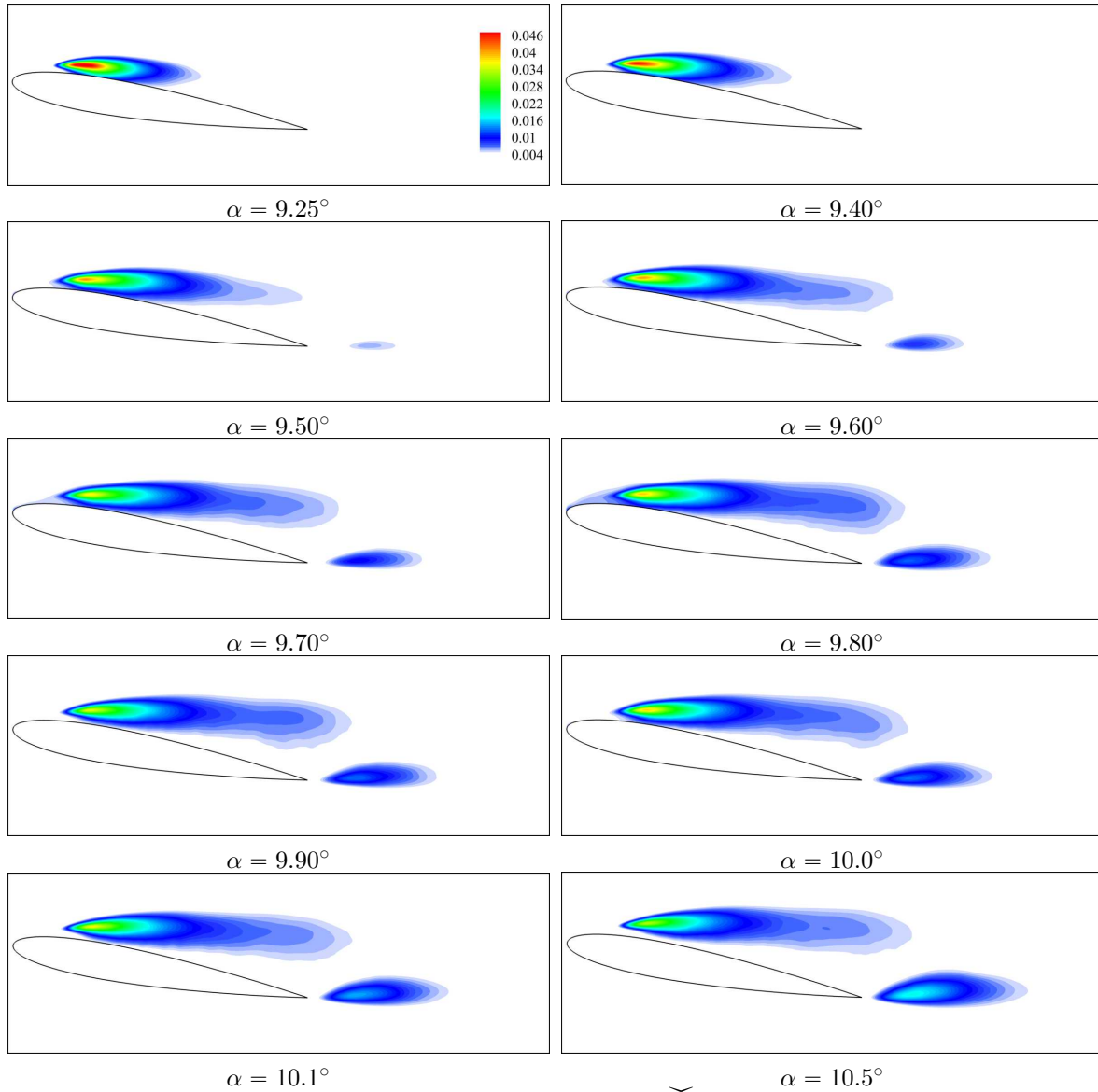


Figure 26. Colours map of the low-lift variance of the pressure, $\overline{p''^2}$, for the angles of attack $\alpha = 9.25^\circ$ – 10.5° .

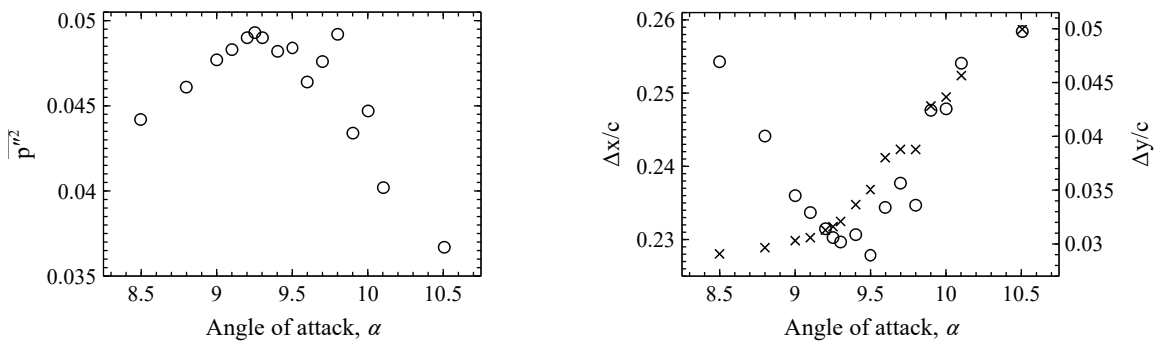
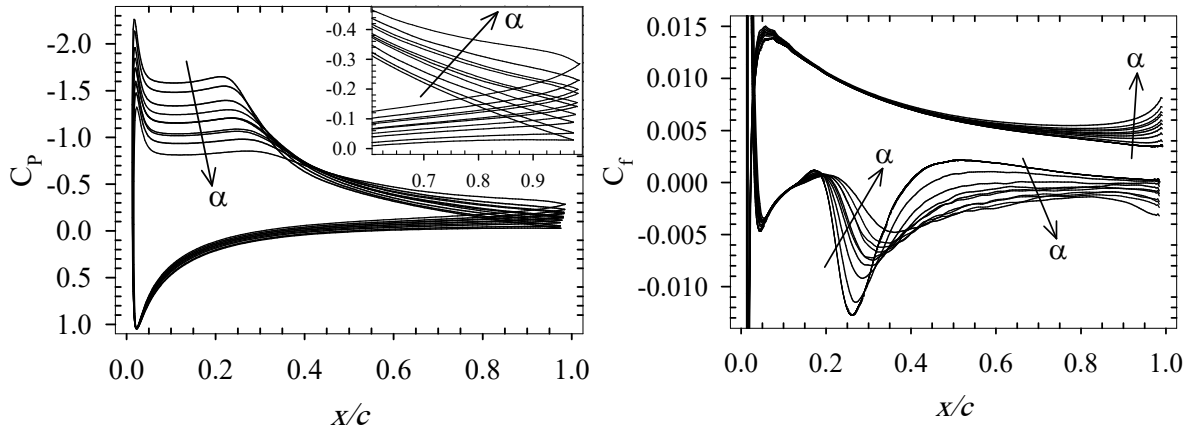


Figure 27. Left: the maximum $\overline{p''^2}$ plotted versus the angle of attack α . Right: the locations of the maximum $\overline{p''^2}$ plotted versus the angle of attack α . Circles: $\Delta x/c$ measured from the aerofoil leading-edge, \times 's: $\Delta y/c$ measured from the aerofoil surface.



The local pressure coefficient C_p .

The local skin-friction coefficient C_f .

Figure 28. Locally-time-averaged pressure and skin-friction coefficients for the angles of attack $\alpha = 9.25^\circ$ – 10.5° . The arrows indicate the direction in which the angle of attack, α , increases in ascending order.

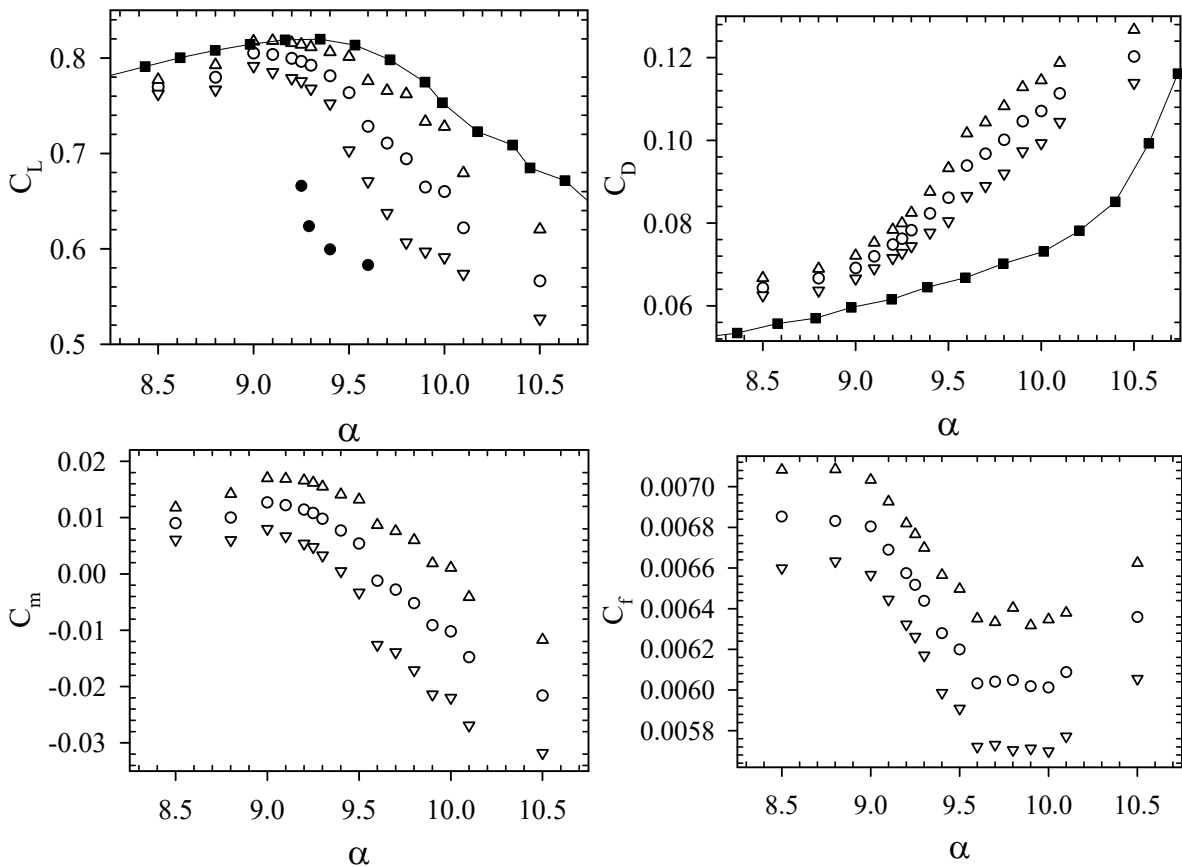


Figure 29. Mean aerodynamic coefficients C_L , C_D , C_m , and C_f plotted versus the angle of attack α . Circles: mean ($\bar{\cdot}$), upward triangles: high-lift mean ($\bar{\cdot}$), downward triangles: low-lift mean ($\bar{\cdot}$), solid line with filled black squares: the experimental data of Ohtake *et al.* (2007) at $Re_c = 5 \times 10^4$ transformed to its corresponding compressible counterpart.

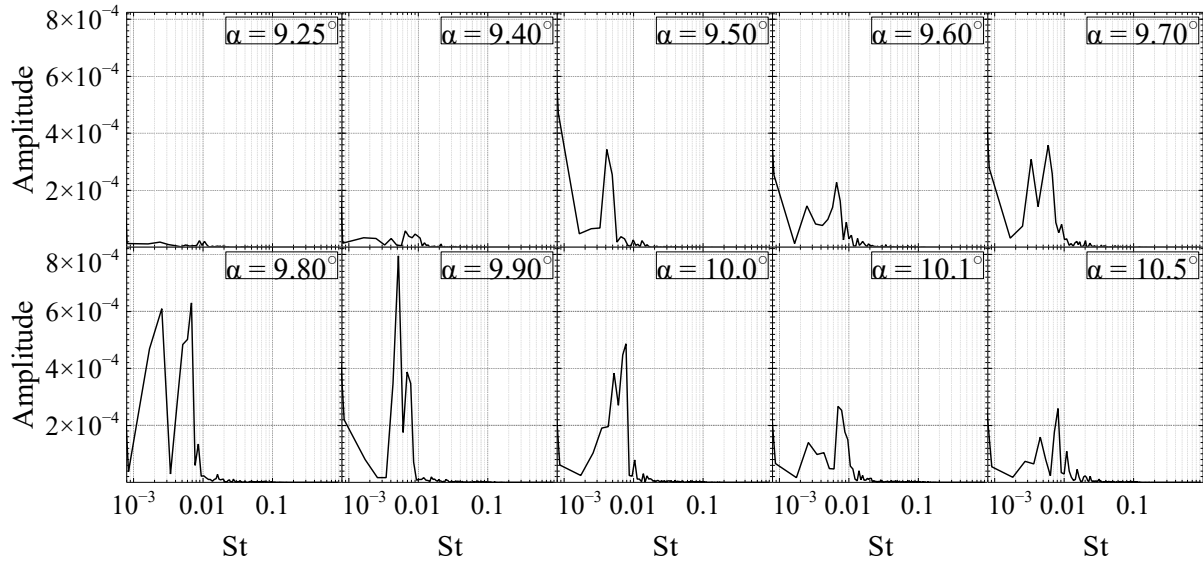


Figure 30. Spectra of the lift coefficient for the angles of attack $\alpha = 9.25^\circ$ – 10.5° .

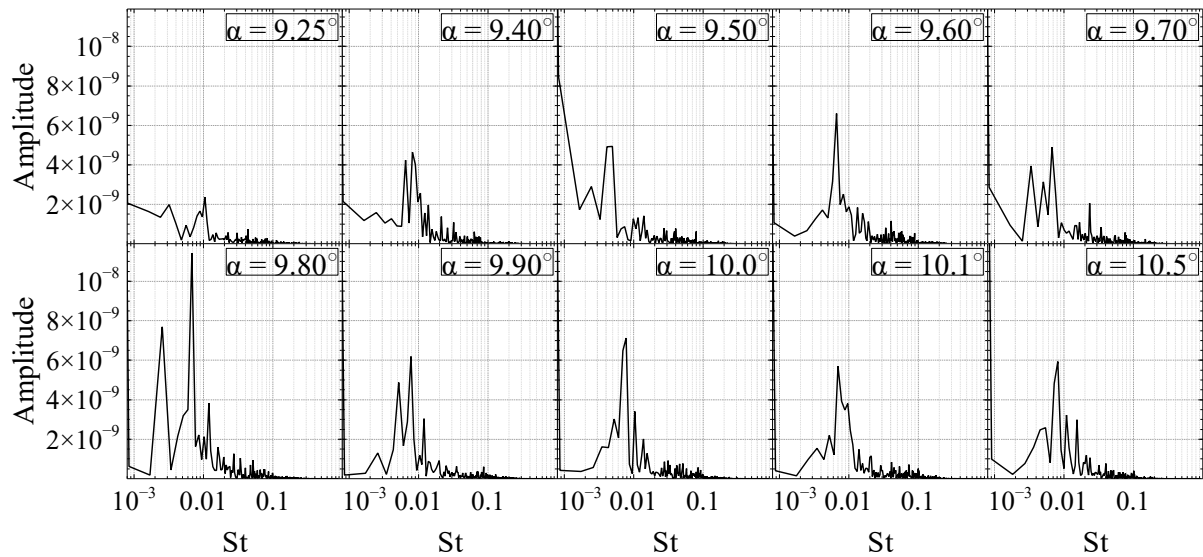
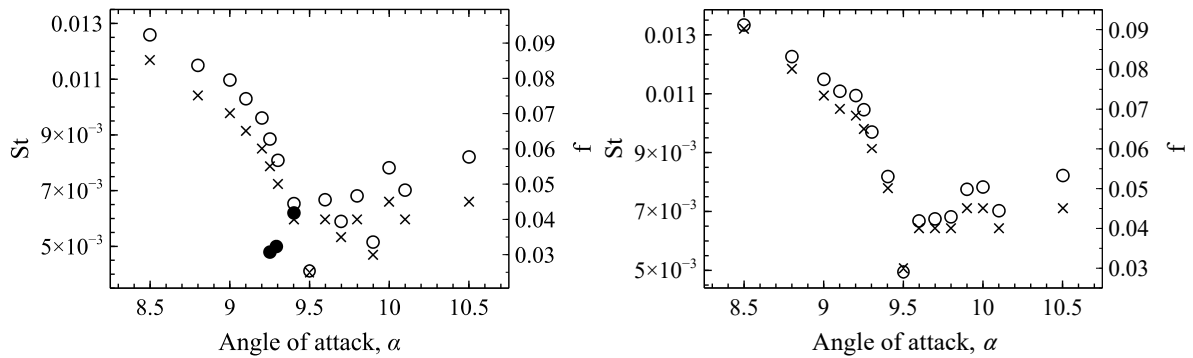


Figure 31. Spectra of the skin-friction coefficient for the angles of attack $\alpha = 9.25^\circ$ – 10.5° .



The lift coefficient.

The skin-friction coefficient.

Figure 32. Low-frequency Strouhal number (St) and non-dimensional frequency (f) plotted versus the angle of attack. Circles: Strouhal number, \times 's: non-dimensional frequency, filled black circles: the LES data by Almutairi & Alqadi (2013).